Neutron observables from inclusive lepton scattering on nuclei

A. S. Rinat and M. F. Taragin
Weizmann Institute of Science, Department of Particle Physics, Rehovot 76100, Israel
(Received 21 March 2010; published 27 July 2010)

We analyze new data from Thomas Jefferson National Accelerator Facility (JLab) for inclusive electron scattering on various targets. Computed and measured total inclusive cross sections in the range $0.3 \lesssim x \lesssim 0.95$ show reasonable agreement on a logarithmic scale for all targets. However, closer inspection of the quasielastic components reveals serious discrepancies. European Muon Collaboration (EMC) ratios with conceivably smaller systematic errors fare the same. As a consequence, the new data do not enable the extraction of the magnetic form factor G_M^n and the structure function F_2^n of the neutron, although the application of exactly the same analysis to older data had been successful. We incorporate in the above analysis older CLAS Collaboration data on $F_2^{^2\mathrm{H}}$. Removal of some scattered points from those makes it appear possible to obtain the desired neutron information. We compare our results with others from alternative sources. Special attention is paid to the $A = 3$ isodoublet cross sections and EMC ratios. Present data exist only for ^{3}He, but the available input in combination with charge symmetry enables computations for ^{3}H. Their average is the computed isoscalar part and is compared with the empirical modification of ^{3}He EMC ratios toward a fictitious $A = 3$ isosinglet.

DOI: 10.1103/PhysRevC.82.015207 PACS number(s): 25.30.Fj, 25.30.Rw, 13.40.Gp, 13.60.Hb

I. INTRODUCTION

Nearly a decade has passed since the publication of Thomas Jefferson National Accelerator Facility (JLab) experiment E89-008, describing inclusive scattering of electrons on various targets [1,2]. Those extended older SLAC data on ^{2}H and He isotopes [3] and later ones for beam energies $E \leqslant 3.6$ GeV on ^{2}H, ^{4}He, and several medium and heavy targets [4]. A similar experiment in 1999 used $E = 4.05$ GeV electrons [5].

In the JLab experiments E03-102 and E02-90, 5.76 GeV unpolarized electrons were scattered over angles $\theta = 18^\circ, 22^\circ, 26^\circ, 32^\circ, 40^\circ$, and 50°. Total inclusive cross sections covering wide kinematics have been measured for targets ^{2}H, ^{3,4}He, ^{9}Be, C, Al, and Cu. From this extensive data bank, only the European Muon Collaboration (EMC) ratios $\mu^{^{3,4}\mathrm{He}}$, μ^{Be}, and μ^{C} for one scattering angle $\theta = 40^\circ$ and limited kinematics have been published until now [6]. In addition, cross section data over the entire measured kinematic range and for all targets have been made available [7]. We also mention data taken with an $E = 5.0$ GeV beam, the analysis of which has not yet been completed [8].

In order to define notation, we start with the total cross section per nucleon for inclusive scattering of unpolarized electrons, reduced by the Mott cross section σ_M. For given beam energy E, scattering angle θ, and energy loss ν, one has

$$K^A(x, Q^2, \theta) = \frac{d^2\sigma^A(E;\theta,\nu)}{d\Omega\, d\nu} \Big/ \sigma_M(E;\theta,\nu) = \frac{2xM}{Q^2} F_2^A(x, Q^2) + \frac{2}{M} F_1^A(x, Q^2)\tan^2(\theta/2). \tag{1.1}$$

$F_{1,2}^A(x, Q^2)$ above are nuclear structure functions (SFs), which depend on the squared four-momentum transfer $q^2 = -Q^2 = -(|\boldsymbol{q}|^2 - \nu^2)$ and the Bjorken variable $0 \leqslant x = Q^2/2M\nu \leqslant M_A/M \approx A$ with M the nucleon mass.

Several approaches have been proposed for an analysis of inclusive cross sections in the plane-wave impulse approximation (PWIA), or the same with some final-state interaction (FSI) distortions [9,10]. We report here on an analysis based on a previously tested nonperturbative Gersch-Rodriguez-Smith (GRS) approach [11,12]. Our application also covers the entire corpus of new data (ND) beyond the restricted targets and kinematics of the published material reported in Refs. [6,7]. To those we add an analysis of ^{2}H CLAS (CL) data [13]. Except for the treatment of the $A = 3$ targets, the method of analysis for the new data is identical to that previously applied to the older data (OD). We therefore shall not detail steps but mention references instead.

We adhere in the following to a generalized convolution, linking F_k^A and $F_k^{p,n}$ (see, for instance, Ref. [11]),

$$F_k^A(x, Q^2) = \int_x^A \frac{dz}{z^{2-k}} \left[f_p^A(z, Q^2) Z F_k^p\left(\frac{x}{z}, Q^2\right) + f_n^A(z, Q^2) N F_k^n\left(\frac{x}{z}, Q^2\right)\right] \Big/ A. \tag{1.2}$$

$$\approx \int_x^A \frac{dz}{z^{2-k}} f^A(z, Q^2) \left[Z F_k^p\left(\frac{x}{z}, Q^2\right) + N F_k^n\left(\frac{x}{z}, Q^2\right)\right] \Big/ A. \tag{1.3}$$

The f^A here are SFs for a fictitious nucleus composed of point particles which cannot be excited, irrespective of the value of Q^2 [14]. Alternatively, one interprets f as a kind of generalized distribution function of the centers of interacting nucleons in a target.

The functions f^A for finite Q^2 can be calculated exactly only for the lightest nuclei and have otherwise to be modeled [11]. In the PWIA the above norm can be shown to be 1. The same is expected for any bona fide distribution function. We shall return to this point in detail.

In virtually all previous applications one did not distinguish between distribution functions $f_{p,n}^A$, which are different for p and n. However, in a treatment of the lightest odd nuclei, their

difference may matter and a proper treatment ought to use Eq. (1.2).

Equations (1.2) and (1.3) feature nucleon SFs $F_k^{p,n}$, which in general are off their mass shell. However, in the region of our main $Q^2 \gtrsim (2.5\text{–}3.0)$ GeV^2, those effects may be neglected, and the same holds for the mixing of nucleon SFs in the proper expression for F_2^A [15,16]. Since the data do not reach the deepest inelastic range $x \lesssim 0.2$, screening effects may also be disregarded [17]. For $Q^2 \lesssim 3.0$ GeV^2, for which (pseudo)resonance structure is not yet extinguished, we shall use F_2^p from Ref. [18], while for larger Q^2 we rely on a parametrization of the resonance-averaged F_2^p [19]. References to F_2^n can be found in [11].

It is convenient to decompose the nucleon SFs F_k^N in Eq. (1.2) into parts, describing the absorption of a virtual photon, either exciting the absorbing N into hadrons (partons) or not ($\gamma^* + N \to N$). The amplitudes for the latter vanish except for $x = 1$, in which case those may be expressed as standard combinations of electromagnetic form factors (FFs). A similar division applies to nuclear SFs. Denoting by $[\tilde{G}^N]^2 = [Z(G^p)^2 + N(G^n)^2]/A$ the (Z, N)-weighted average of the squared nucleon FFs, one finds from Eq. (1.3) their nuclear analogs [$\eta = Q^2/(4M^2)$]

$$F_1^{A,\mathrm{NE}}(x, Q^2) = \frac{f^{PN,A}(x, Q^2)}{2}\left[\tilde{G}_M^N(Q^2)\right]^2, \tag{1.4}$$

$$F_2^{A,\mathrm{NE}}(x, Q^2) = x f^{PN,A}(x, Q^2)\frac{\left[\tilde{G}_E^N(Q^2)\right]^2 + \eta\left[\tilde{G}_M^N(Q^2)\right]^2}{1+\eta}. \tag{1.5}$$

Nuclear inelastic (NI) processes dominate in general, but occasionally one needs to include the above quasielastic parts (NE).

In inclusive spectra one distinguishes the following kinematic regions:

(i) Deepest inelastic scattering for $x \lesssim 0.2$, with characteristic (anti)screening effects.
(ii) The NI-dominated deep inelastic scattering (DIS) region, $0.2 \lesssim x \lesssim x_r(Q^2)$ with $x_r(Q^2) \approx [(M_R^2 - M^2)/Q^2 + 1]^{-1}$, with the Bjorken x for resonance excitation.
(iii) The NI-NE interference region for $x_r(Q^2) \lesssim x \lesssim 0.85$–$0.95$.
(iv) The quasielastic (QE) region around the quasielastic peak (QEP), $0.95 \lesssim x \lesssim 1.05$, dominated by NE processes, and only weakly perturbed by NI tails, provided $Q^2 \lesssim (4\text{–}5)$ GeV^2.
(v) The deep quasielastic (DQE) region, $x \gtrsim 1.05$, dominated by NE processes. Cross sections there are very small in comparison with those in regions (i)–(iv) and again are for not too high Q^2, only weakly perturbed by inelastic tails.

In the following, all measured total cross sections, whether published as EMC ratios of the above in a limited kinematic range, or as yet unpublished results for the entire measured kinematic ranges [6,7], will be referred to as "data."

This paper is organized as follows. We first report in Sec. II A on general features of total inclusive cross sections, which we illustrate by a few examples for isosinglet targets. From a comparison of experimental and computed total cross sections over the larger part of the kinematic x range $0.35 \lesssim x \lesssim 0.95$, we conclude that in the DIS region NI components are apparently reliably computed.

For increasing x toward the QE region, NE components grow, start to compete with NI, and for not too large Q^2, finally overtake them. We show that around the QEP and in both wings, theory and data for NE components applied to ND almost never agree.

Particular attention is paid to the $A = 3$ isodoublet, where we distinguish between p and n as struck nucleons (Sec. II B). Section II C deals with EMC ratios derived from the material in Secs. II A and II B. Since in the only publication thus far the prime interest is a sample of EMC ratios for the lightest nuclei in the classical EMC region $x_{\min}^{\mathrm{data}} \lesssim x \lesssim 0.9$, a comparison with computed results, including for ^{3}He, is limited to those.

In Sec. III we focus on the QE region and try to extract the reduced magnetic FF $\alpha_n = G_M^n/(\mu_n G_d)$ (G_d). We apply a previously formulated criterion, which has to be satisfied before one can attempt an extraction. For ND it appears virtually never fulfilled.

As an alternative source, we include in Sec. III the CLAS data for $F_2^{^2\mathrm{H}}$ [13]. If a few manifestly scattered data points in the QE region are removed, the above-mentioned criterion is satisfactorily met by the CLAS data, which we endowed with (2–3)% systematic errors. We shall show that the extracted averaged reduced neutron magnetic FFs α_n agree with the OD results.

In Sec. IV we exploit the same CL data in order to extract the neutron SF F_2^n along lines used in the past [20]. In the concluding section we discuss both theoretical and experimental aspects of the extraction of n properties from inclusive cross sections.

II. CROSS SECTIONS AND DERIVED OBSERVABLES

A. Total inclusive cross sections

Total inclusive cross sections are usually computed from forms like Eq. (1.3), with $f^A(x, Q^2)$ in some approximation, for instance the PWIA (or the distorted-wave inpulse approximation), or on the light cone. Below we adhere to a nonperturbative GRS theory, which we have exploited over years [11,12]. Obviously, starting from one given Hamiltonian, different approaches evaluated to sufficiently high order in suitable expansion coefficients should ultimately tend to the same final results [21]. Our choice of the GRS approach is only motivated by, in general, better convergence of low-order terms.

We start with an outline of the derivation for $f_p = f_n$, referring for details to Refs. [11,12] and [22]. In Eq. (2.8) of the last reference we mentioned and discussed the GRS expansion

$$\phi(q, y_G) = \sum_n \left(\frac{M}{q}\right)^n \phi_n(y_G) \tag{2.1}$$

of a related function $\phi(q, y_G)$ of $q = |\vec{q}|$, the three-momentum along the z axis, and of a relativistic generalization of the

nonrelativistic West scaling variable [23] ($\eta = Q^2/4M^2$)

$$y_G = y_G^\infty \left(1 - \frac{1-x}{2(A-1)(1+x^2/\eta)}\right),$$
$$y_G^\infty = \frac{M}{(1+x^2/\eta)^{1/2}}(1-x).$$

y_G^∞ is the West variable for an infinitely heavy recoiling spectator. We now abbreviate y_G by y.

In the following we retain only the two lowest-order terms in the GRS series (2.1),

$$\phi^{A;\mathrm{GRS}}(q,y) \approx \phi^{A;(0)}(q,y) + (M/q)\phi^{A;(1)}(q,y). \tag{2.2}$$

The lowest-order term is expressed by means of the single-hole spectral function of the target (SPFT) $S(E,k)$ [Ref. [22], Eq. (2.9)] and the second term describes the dominant FSI.

The appearance of SPFTs in expressions for the lowest-order SF is common to all approaches. Those are mainly distinguished by the definition or choice of the fourth component of the missing four-momentum. For instance, in the GRS theory the latter is determined by the requirement that the ejected N and the spectator shall, to equal measure, be off their mass shells [23]. Its contribution $\tilde{\phi^{(0)}}$ is detailed in Ref. [12], Eqs. (66) and (67).

The next-order GRS term for the usually dominant FSI reads [cf. Ref. [22], Eq. (2.17a)]

$$(M/q)\phi^{A;(1)}(y,q) = (M/q)\int_0^\infty \frac{ds}{2\pi} e^{isy} \iint d\vec{r}_1 d\vec{r}_2 \rho_2^A(\vec{r}_1,\vec{r}_2;\vec{r}_1',\vec{r}_2) \times [i\tilde{\chi}_q^A(\vec{b},z;s)], \tag{2.3}$$

and contains two components. The first is a two-particle density matrix ρ_2, not diagonal in one coordinate, which in principle may be obtained from the product of two A-particle ground-state wave functions, integrating out $A-2$ coordinates. For $A > 4$ one usually makes a shortcut, using an interpolating approximation [11]

$$\rho_2^A(\vec{r}_1,\vec{r}_2;\vec{r}_1',\vec{r}_2) \approx \rho_1^A(r_1)\rho_1^A(r_2)\left(\frac{\rho_1^A(r_1,r_1')}{\rho_1^A(r_1)}\right) \times \sqrt{g^A(|\vec{r}_1-\vec{r}_2|)g^A(|\vec{r}_1'-\vec{r}_2|)}, \tag{2.4}$$

where $\rho_1^A(1,1) = \rho_1^A(1)$ and g^A are the single-particle density and the pair-distribution function. Using the Negele-Vautherin ansatz [24], the nondiagonal single-particle density $\rho_1^A(\vec{r}_1,\vec{r}_1')$ is computed from

$$Y^A(s) \equiv \frac{\rho_1^A(\vec{r}_1,\vec{r}_1')}{\rho_1^A(r_1)} \approx \int \frac{d^3k}{(2\pi)^3} e^{i\vec{k}\cdot\vec{s}} n^A(k) = \frac{1}{2\pi^2 s}\int_0^\infty dk\, k\sin(ks) n^A(k). \tag{2.5}$$

$n^A(k)$ is the single-particle momentum distribution, obtained by integrating the SPFT over the missing energy E,

$$n^A(k) = \int_0^\infty dE\, S^A(k,E) \tag{2.6}$$

The second factor in the integrand in (2.3) is an off-shell phase factor $\tilde{\chi}_q(\vec{b},z;s)$ in terms of the relative coordinates $\vec{r}_1 - \vec{r}_2 = (\vec{b},z)$; $\vec{s} \equiv \vec{r}_1 - \vec{r}_1' = (\vec{q}/|q|s)$. The appended $q \approx |\vec{p}+\vec{q}|$ is approximately the laboratory momentum of the nucleon, which absorbed the virtual photon, before a FSI scattering from another N occurs.

In Ref. [22], Eqs. (2.17b)–(2.21b), we discuss the approximation

$$i\tilde{\chi}_q(\vec{b},z) \approx \theta(z)[\theta(s-z) - s\delta(s-z)]\Gamma_q(b), \tag{2.7}$$

with the standard on-shell profile function $\Gamma_q^{(1)}(b) = -(\sigma_q^{\mathrm{tot}}/2)(1-i\tau_q)A_q(b)$. It is related to the diffractive elastic NN scattering amplitude f_q^{NN}, with $\tau_q = \mathrm{Re}\, f_q/\mathrm{Im}\, f_q$ and $A_q(b) = [Q_q(0)]^2/4\pi]e^{-(bQ_q^{(0)})^2/4}$. With np and pp data of quite different quality, one usually takes an average of the relevant np and pp cross sections [11].

Next one transforms the representative terms $\phi(q,y_G)$ in the GRS expansion (2.2) by means of a Jacobian

$$J^A(x,Q^2) = |\partial y^A/\partial x| \approx M\left(\frac{1+x/\eta}{(1+x^2/\eta)^{3/2}}\right) \times \left|1 - \frac{(1-x)(2+3x/2\eta - x^2/\eta)}{2(A-1)(1+x/\eta)(1+x^2/\eta)}\right| \tag{2.8}$$

to the distribution function f^A in the x, Q^2 variables,

$$\phi^A(q,y) \to f^A(x,Q^2) = J^A(x,Q^2)\phi^A(q(x,Q^2),y^A(x,Q^2)). \tag{2.9}$$

By means of those distribution functions f^A one computes the SFs $F_k^A(x,Q^2)$ in Eq. (1.3), and in particular the inelastic parts $\mathrm{NI}^{\mathrm{calc}}$ [11,25]. The elastic NE components are expressed in terms of FFs and the computed distribution functions $f^A(z,Q^2)$ as in Eqs. (1.4) and (1.5). Their sum defines total cross sections

$$\sigma^{A,\mathrm{tot}} = \mathrm{NI}^{\mathrm{calc}} + \mathrm{NE}^{\mathrm{FF}}. \tag{2.10}$$

We applied this to all E03-102 and E02-90 total cross section data.

In view of the fact that only a restricted part of the measured ND have been published, we first display in Figs. 1(a)–1(d) and 2(a)–2(d) a sample of $I = 0$ targets, namely, ^{2}H($\theta = 18^\circ, 22^\circ, 26^\circ, 32^\circ$) and C ($\theta = 26^\circ, 32^\circ, 40^\circ, 50^\circ$). These are shown as heavy lines, to be distinguished from heavy dots for data, first shown without error bars.

With the exception of remnants of resonance excitations of the lightest nuclei at low θ (i.e., low Q^2), the examples of smooth data shown are typical for all targets $A \geqslant 12$ at similar kinematics.

A cursory glance at the logarithms of the above total cross sections shows reasonable agreement for each scattering angle and target, in particular for the smallest x measured. This holds down to the approach to the resonance region, where $\mathrm{NI}^{\mathrm{calc}} \gg$ NE. The read-off agreement thus provides evidence that the calculated NI components in the DIS region are basically correct. In contrast, when we move to the QE and DQE regions, growing discrepancies occur in very small cross sections. In order to understand the nature of the above discrepancies, we separately consider NE and NI components.

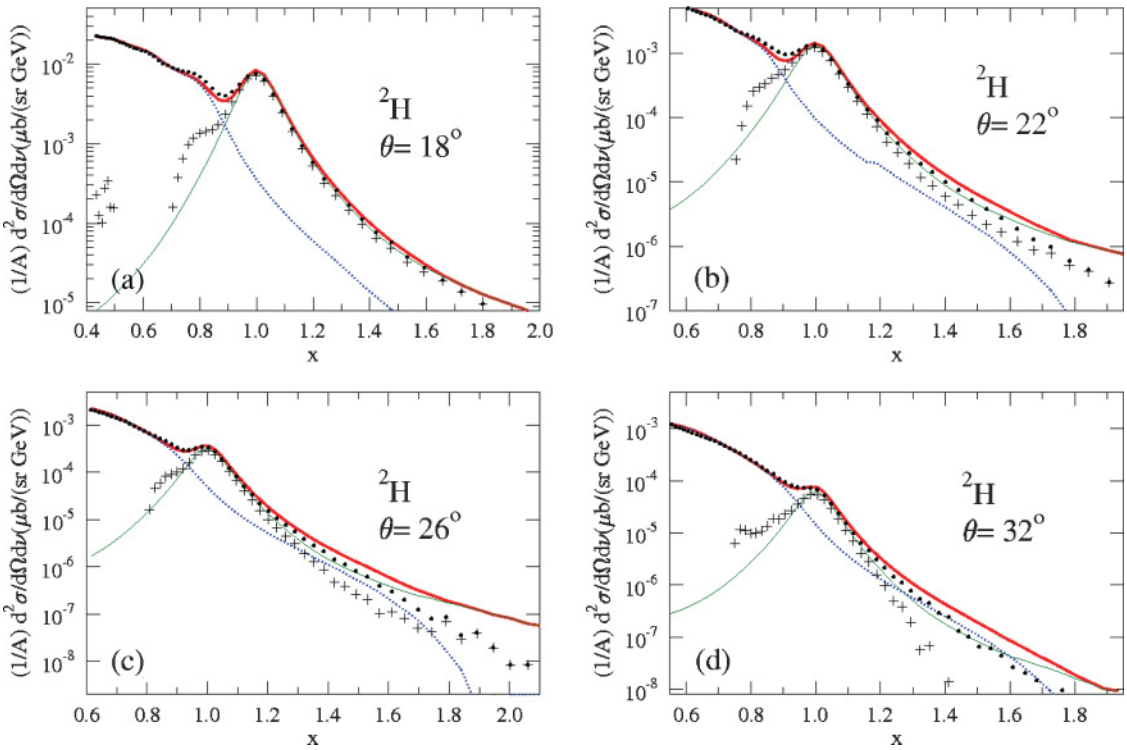

FIG. 1. (Color online) $\sigma^{\rm tot}$ for inclusive scattering of $E = 5.76$ GeV electrons on ^{2}H; (a)–(d) are for $\theta = 18^\circ,\ 22^\circ,\ 26^\circ,$ and 32°. Heavy dots are data without error bars. Small dots (blue) and thin line (green) are NI$^{\rm calc}$ and NE$^{\rm FF}$, Eqs. (1.3), (1.4), and (1.5). Heavy line (red) is their sum. Crosses are NE$^{\rm extr}$ = data – NI$^{\rm calc}$, Eq. (2.11). Missing crosses indicate data $\leqslant$ NI$^{\rm calc}$.

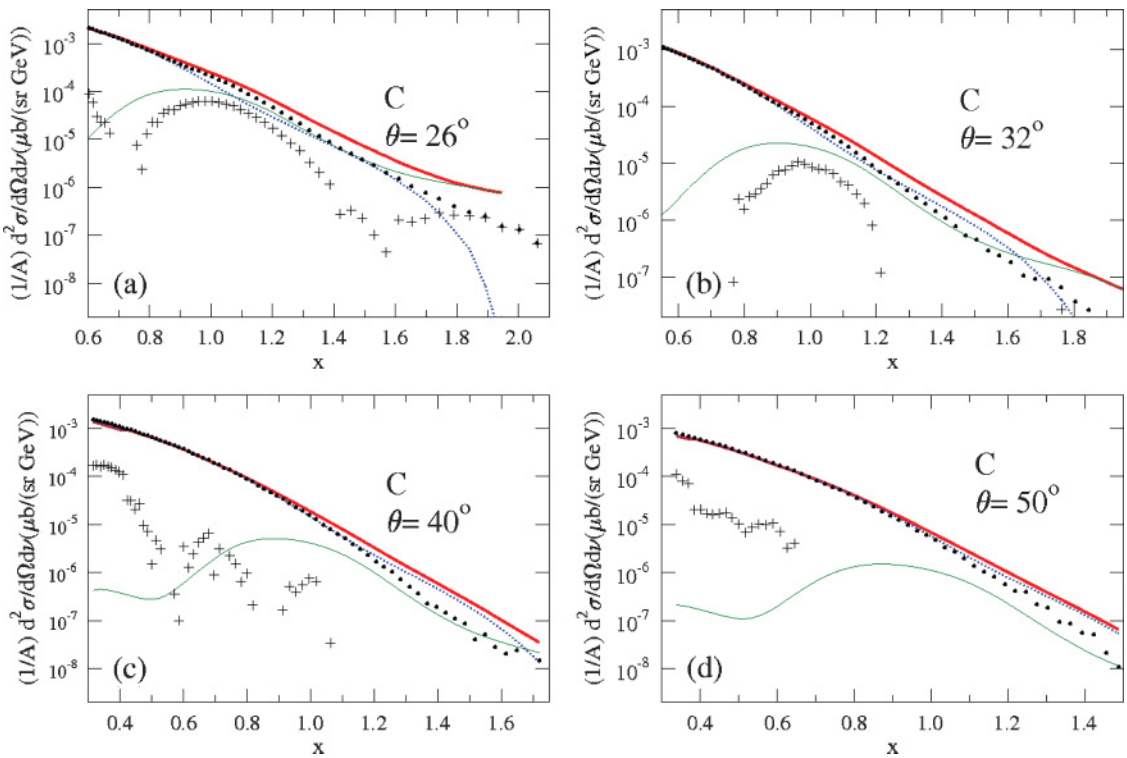

FIG. 2. (Color online) As Fig. 1 for C. (a)–(d) are for $\theta = 26^\circ,\ 32^\circ,\ 40^\circ,$ and 50°.

In addition to the computed $\mathrm{NE}^{\mathrm{FF}}$, Eqs. (1.4) and (1.5), we define

$$\mathrm{NE}^{\mathrm{extr}} = \mathrm{data} - \mathrm{NI}^{\mathrm{calc}}. \tag{2.11}$$

Clearly, the semiempirical $\mathrm{NE}^{\mathrm{extr}}$ will show the scatter present in the data, while $\mathrm{NE}^{\mathrm{FF}}$ in $\sigma^{A,\mathrm{tot}}$, Eq. (2.10), is a smooth function of x, f^A, and FFs. For perfect data and theory the NE values from Eqs. (1.5) and (2.11) should coincide.

The expression $\mathrm{NE}^{\mathrm{FF}}$ in the single-photon exchange (SPE), Eq. (1.5), uses among other things G_E^p. The primary discrepancy is in the ratio $\gamma = \mu_p G_E^p / G_M^p$, once measured in a Rosenbluth separation, and then by polarization transfer [26]. It has led to calculations of two-photon exchange (TPE) corrections on an isolated p [27,28]. Those have been shown to reduce the discrepancy mentioned above.

The above TPE corrections have been parametrized in the functional form of a SPE part, which enables the sum SPE + TPE to be considered as an effective SPE [28]. All results in the following use that input. Their effect on a single bound p appears to change σ^A for "bare" SPE by less than 1%. There also exist TPE corrections involving two nucleons, and so on, but their contributions have as yet not been determined.

We return to Figs. 1(a)–1(d) and 2(a)–2(d), where we display $\mathrm{NI}^{\mathrm{calc}}$ (light dots) and $\mathrm{NE}^{\mathrm{FF}}$ (light drawn lines), as well as their calculated sum $\sigma^{A,\mathrm{tot}}$. Crosses in these figures represent $\mathrm{NE}^{\mathrm{extr}}$, Eq. (2.11), and these are seen to differ considerably from $\mathrm{NE}^{\mathrm{FF}}$. Missing crosses indicate that $\mathrm{NI}^{\mathrm{calc}}$ locally exceeds data.

For growing x, NE contributions increasingly compete with NI and eventually dominate, and we thus focus on the QE region. Although on a logarithmic scale a small number of points in the QE regions may occasionally seem to be close to the dotted lines, actual discrepancies come to the fore on linear plots for $\mathrm{NE}^{\mathrm{PP}}$ together with $\mathrm{NE}^{\mathrm{extr}}$. The latter now include total error bars, where we added to statistical errors (2–3)% estimates for systematic ones. Figures 3(a)–3(d) are samples for ^{2}H(18,40) and C(18,40). Discrepancies appear to grow with both A and Q^2 and are occasionally quite erratic. Clearly the ND cross sections and the results of standard computations are at odds.

This is not the case for the analysis of the OD, using the same code. We illustrate this by a comparison with Figs. 4(a)–4(c) for $\sigma\,^2\mathrm{H}(E = 4.045\ \mathrm{GeV}; \theta = 15^\circ, 30^\circ, 55^\circ)$, taken from Ref. [25]. The logarithmic scale and Bjorken value on the vertical and horizontal scales, as well as symbols and curves, correspond to those in Figs. 1 and 2. We added dashed curves for empirical inelastic NI parts, which cause $\mathrm{NE}^{\mathrm{PP}} \approx \mathrm{NE}^{\mathrm{extr}}$. In the critical region between the QEP and the (first) resonance, $\mathrm{NI}^{\mathrm{emp}}$ exceeds $\mathrm{NI}^{\mathrm{comp}}$ by less than 15%. It is obvious that in the QE region OD and computed results agree far better than is the case for the ND. We shall return to this issue in the Discussion.

B. The $A = 3$ isodoublet

Among the ND are also the first results for ^{3}He after the old SLAC data [3]. Those are of particular interest, since ^{3}He is the lightest stable odd nucleus with a large relative nucleon excess. Approximate charge symmetry invites a simultaneous study of ^{3}He and ^{3}H, although for the latter there are as yet no data.

We thus separately treat $N = p, n$ and start with the lowest-order term $\phi^{A;(0)}$, given in Ref. [22], Eq. (2.9) [or equivalently Eqs. (66) and (67) in Ref. [12]]. This clearly demands knowledge of SPFTs $S_N^{A=3}$ for the ejected nucleon $N = p, n$. In those one distinguishes between a two-body continuum and the ^{2}H spectator state. The latter occurs only if $I_3^{A=3} = I_3^N$ for the three components of the isospins.

Using $\psi_n^{A=2}$ for spectator states with separation energy $\mathcal{E}_n^{A=2}$, one writes for the SPFT and momentum distribution $n^{A=3}(k) = \int_{E_{\min}} dE$, $S^{A=3}(k, E)$ of an $A = 3$ nucleus,

$$\begin{aligned} S^{I_3^{A=3}}(k, E) = & \sum_{j\neq{}^2\mathrm{H}} \left|\left\langle \Psi_0^{I_3^{A=3}} \middle| \Psi_{j\neq{}^2\mathrm{H}}^{I_3^{A=2}} * \vec{k}; I_3^N \right\rangle\right|^2 + \delta\left(E - \mathcal{E}_{j=^2\mathrm{H}}^{A=2}\right) \\ & + \delta\left(I_3^{A=3}, I_3^N\right) \left|\left\langle \Psi_0^{I_3^{A=3}} \middle| \Psi^{^2\mathrm{H}} * \vec{k}; I_3^N \right\rangle\right|^2 \\ & \times \delta(E + B_{^2\mathrm{H}}) \end{aligned} \tag{2.12}$$

$$\begin{aligned} n^{I_3^{A=3}}(k) = & \sum_{j\neq{}^2\mathrm{H}} \left|\left\langle \Psi_0^{I_3^{A=3}} \middle| \Psi_{j\neq{}^2\mathrm{H}}^{I_3^{A=2}} * \vec{k}; I_3^N \right\rangle\right|^2 \\ & + \delta\left(I_3^{A=3}, I_3^N\right) \left|\left\langle \Psi_0^{I_3^{A=3}} \middle| \Psi^{^2\mathrm{H}} * \vec{k}; I_3^N \right\rangle\right|^2, \end{aligned} \tag{2.13}$$

with $B_{^2\mathrm{H}}$ the binding energy of ^{2}H. One then derives the corresponding lowest-order $A = 3$ distribution functions ($\beta = Mv/q$; $\xi = E/M + x - 1$)

$$\begin{aligned} & f_N^{I_3^{A=3};(0)}(x, Q^2) \\ & = \frac{J^{(3)}(x, Q^2)}{4\pi^2} \left[\theta(x-1) \int_0^\infty dE \int_{\beta\xi}^\infty dk\, k S_N^{I_3^{A=3}}(k, E) \right. \\ & \quad + \theta(1-x) * \left(\int_{M(1-x)}^\infty dE \int_{\beta\xi}^\infty dk\, k S_N^{I_3^{A=3}}(k, E) \right. \\ & \quad \left. \left. + \int_0^{M(1-x)} dE \int_{-\beta\xi}^\infty dk\, k S_N^{I_3^{A=3}}(k, E) \right) \right] \\ & \quad + \delta\left(I_3^{A=3}, I_3^N\right) \int_{|y|}^\infty dk\, k n_{N;^2\mathrm{H}}^{A=3}(k), \end{aligned} \tag{2.14}$$

with $y = \lim_{E\to -B_{^2\mathrm{H}}}(\beta\xi)$. $J^{(3)}(x, Q^2)$ above is the Jacobian Eq. (2.8) and

$$n_{N;^2\mathrm{H}}^{A=3}(k) = \int_0^\infty dE\, S_N^{I_3^{A=3}}(k, E)\delta(E + B_{^2\mathrm{H}}), \tag{2.15}$$

the ^{2}H component of the $A = 3$ momentum distribution.

Regarding the dominant FSI term, Eq. (2.3), one distinguishes as before between a nucleon "1" that is a p or an n. In the evaluation the following assumptions will be made:

(i) p and n number densities ρ_1 [29] are equal in either ^{3}He or ^{3}H, but not in both species.

(ii) As to single p and n momentum distributions, we computed $n_{p,n}^{^3\mathrm{He}}(k)$ from the generalization Eq. (2.13) of (2.4) and found small differences for single p and n components.

(iii) In the generalization of Eq. (2.4) we assume $g^{nn}(|\vec{r}_1 - \vec{r}_2|) = g^{pp}(|\vec{r}_1 - \vec{r}_2|)$ and $g^{pn}(|\vec{r}_1 - \vec{r}_2|) = g^{np}$

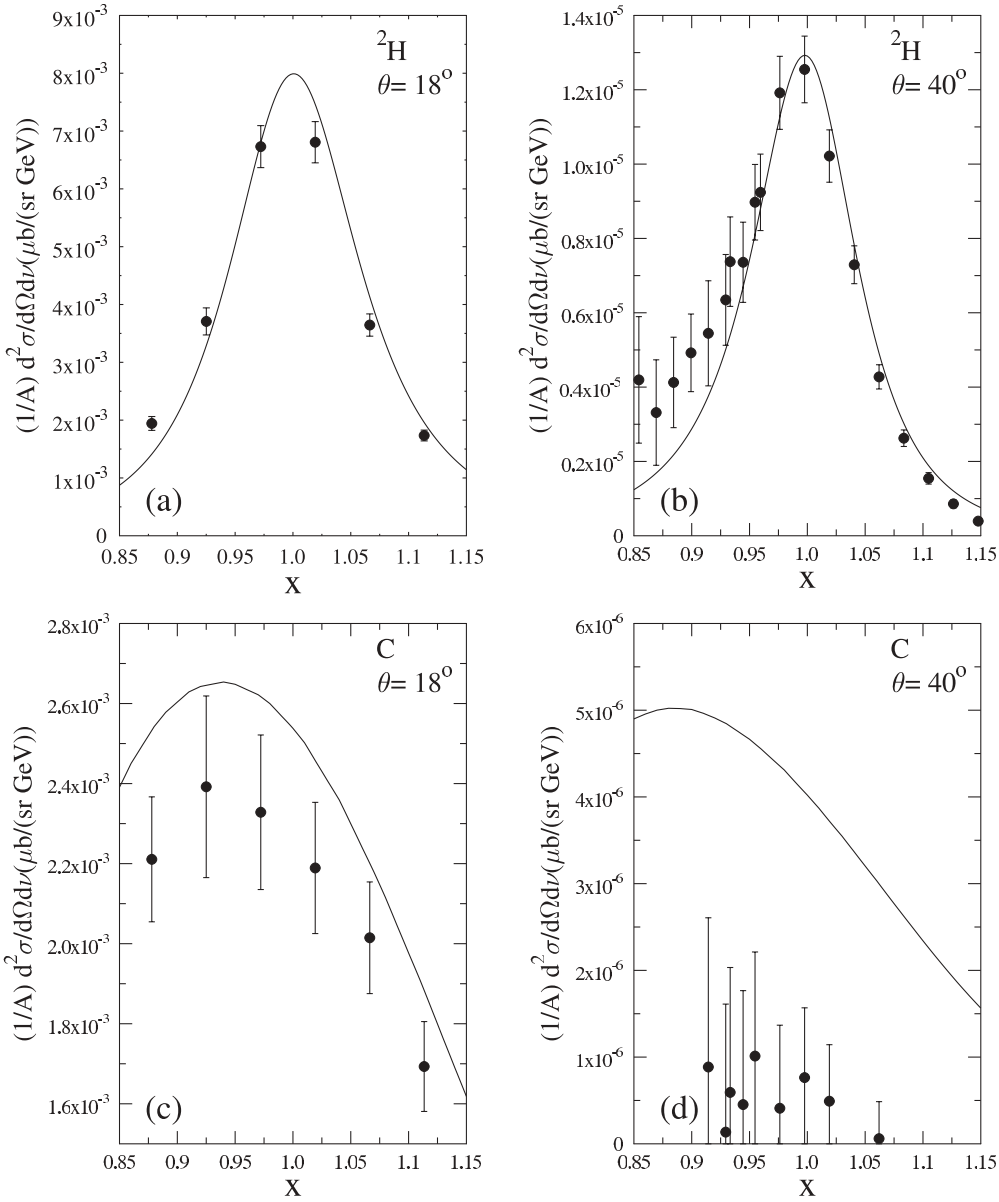

FIG. 3. (a),(b) Linear plots of the QE parts of the total inclusive cross section of $E = 5.76$ GeV electrons on ^{2}H, for $\theta = 18^\circ$ and 40°. (c),(d) Same for C. Legend as for Fig. 1. In addition, drawn lines are NE$^{\rm FF}$, Eqs. (1.3) and (1.4). Filled circles are data with total error bars.

$(|\vec{r}_1 - \vec{r}_2|)$, which change Eq. (2.3) into

$$\begin{aligned}\rho_2^{I_3^{A=3}}(1,2;1'2) \to\ & 1/3[\rho_2(\vec{r}_{1,p},\vec{r}_{2,p};\vec{r}'_{1;p},\vec{r}_{2,p}) \\ & + \rho_2(\vec{r}_{1,p},\vec{r}_{2,n};\vec{r}'_{1,p},\vec{r}_{2,n}) \\ & + \rho_2(\vec{r}_{1,n},\vec{r}_{2,p};\vec{r}'_{1,n},\vec{r}_{2,p})]_{I_3^{A=3}} \\ \approx\ & 1/3[Y(s)\rho_1(\vec{r}_1)\rho_1(\vec{r}_2)]_{I_3^{A=3}}[2\sqrt{g_{pn}(r)g_{pn}(|\vec{r}-\vec{s}|)} \\ & + \sqrt{g_{pp}(r)g^{pp}(|\vec{r}-\vec{s}|)}]. \qquad (2.16)\end{aligned}$$

The functions g_{pp} and g_{pn} have been taken from Ref. [16]. Neglecting the small differences in the single-N momentum distributions $n_N^{I_3^{A=3}}$, the points (i)–(iii) leave no N dependence: $\phi^{A;(1)}$ depends only on $I_3^{A=3}$.

Next we replace $\vec{r}_1, \vec{r}_2$ by relative and center-of-mass system (CMS) coordinates $\vec{r}$, $\vec{R}$ and perform the R integration in (2.3),

$$T(\vec{b},z) = \int d^3\, R\rho_1(|\vec{R}+\vec{r}/2|)\rho_1(|\vec{R}-\vec{r}/2|), \qquad (2.17)$$

which leaves one angular and one radial integration in the expression for $\tilde{\phi}^{(1)}$. Consequently, Y in Eq. (2.16) appears as a factor in

$$\int d\,\vec{R}\rho_2^A(1,2;1',2) \to \frac{1}{3}Y^A(s)T^A(b,z)\mathcal{G}(\vec{b},z;s), \qquad (2.18)$$

with $\mathcal{G}$ a combination of pair-distribution functions in (2.16).

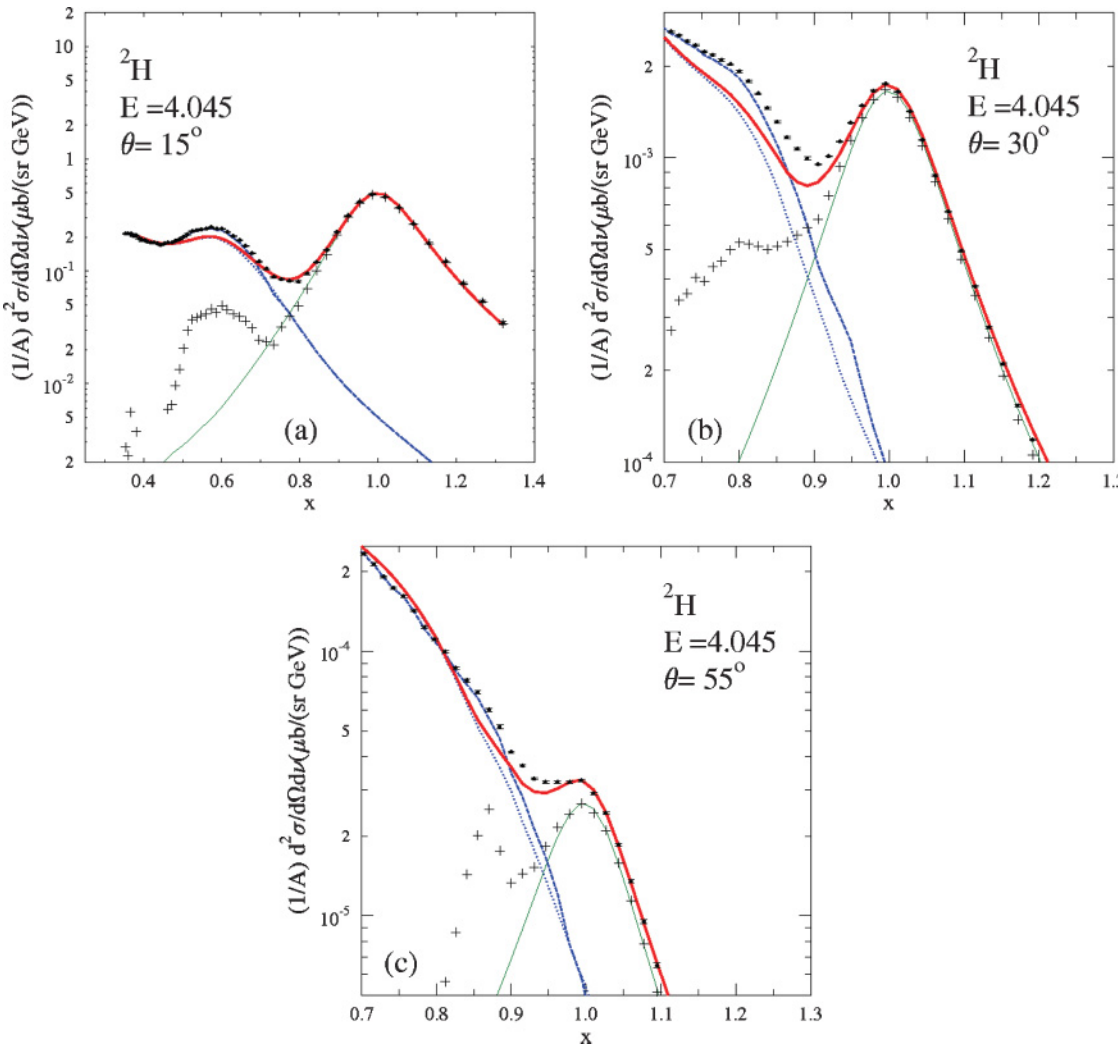

FIG. 4. (Color online) As Fig. 1 for $E = 4.045$ GeV. (a)–(c) are for $\theta = 15^\circ,\ 30^\circ,$ and 45°. In addition to the legend for Fig. 1, dashed curves (blue) are for $\mathrm{NI}^{\mathrm{emp}}$, leading to $\mathrm{NE}^{\mathrm{FF}} \approx \mathrm{NE}^{\mathrm{extr}}$ scale from [25].

Finally, using approximation (2.7) for the phase, the FSI contribution (2.3) becomes

$$\phi^{A=3;(1)}(q, y) = \frac{1}{3}\mathrm{Re}\int_0^\infty ds\, e^{isy} Y(s) \int_0^\infty db\, b \times \left(\int_0^s dz\, [T(b,z)\mathcal{G}(b,z;s)] - sT(b,s)\mathcal{G}(b,s;s)\right), \tag{2.19}$$

where six-dimensional integrals in Eq. (2.3) are reduced to two-dimensional ones. Again, Eq. (2.6) in Ref. [22] produces the corresponding $f^{A=3;(1)}(x, Q^2)$. We checked that $f^{\mathrm{FSI};(1)} \ll f^{(0)}$, but did retain the FSI term $f^{(1)}$ in all calculations.

We now reach the crucial input, which is the outcome of extensive calculations for various SPFTs $S^{^3\mathrm{He}}$, performed by Kievsky *et al.* [30]. Those employed the following NN interactions:

(i) purely two-body NN forces (B2; AV18 [31]), neglecting V_{coul}.

(ii) the same as (i), including V_{Coul}.

(iii) the same as (ii) with an additional $3N$ force (B2 + B3; AV18 UR9 [32]).

The list above does not refer to ^{3}H. All items were intended as input for ^{3}He calculations but clearly only (ii) and (iii) are realistic options with different levels of sophistication. In contrast, option (i) lacks V_{Coul} between protons, that is, the most obvious and dominant charge-symmetry-breaking part, and is therefore not suited for ^{3}H calculations. However, in the absence of other parts, the missing V_{Coul} turns the Hamiltonian for (i) to the the charge-symmetric one corresponding to (ii), that is, for ^{3}H.

However, option (i) is for a ^{3}He Hamiltonian which lacks Coulomb forces between the protons. Thus, disregarding additional charge-symmetry-breaking effect, option (i) describes the isopartner ^{3}H. In particular for the basic distribution functions one has the following relations for the isopartners:

$$f_n^{^3\mathrm{H}} = f_p^{^3\mathrm{He(no\ Coul)}};\ f_p^{^3\mathrm{H}} = f_n^{^3\mathrm{He(no\ Coul)}} \tag{2.20}$$

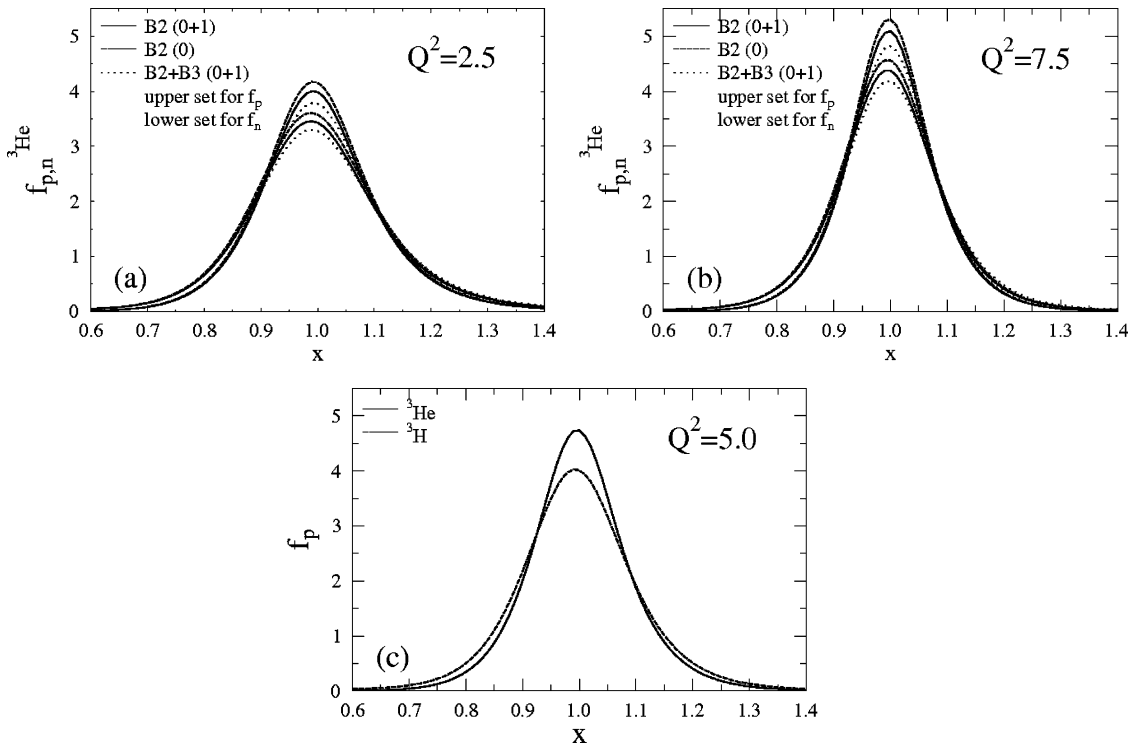

FIG. 5. Distribution functions $f_{p,n}^{^3\mathrm{He}}(x, Q^2)$. (a) and (b) are for $Q^2 = 2.5$ and 7.5 GeV^2. Drawn lines, dashes, and dots correspond to B2(0 + 1), B2(0), and B2 + B3(0 + 1) interactions. (c) is $f_p(x, Q^2 = 5.0\,\mathrm{GeV}^2)$, using B2(0 + 1).

Using Eq. (1.3) one has for the SFs

$$F_2^{^3\mathrm{He}}(x, Q^2) = \int_x^3 dz \frac{1}{3}\left[2f_p^{^3\mathrm{He}}(z, Q^2)F_2^p\left(\frac{x}{z}, Q^2\right) + f_n^{^3\mathrm{He}}(z, Q^2)F_2^n\left(\frac{x}{z}, Q^2\right)\right] \tag{2.21}$$

and either form

$$F_2^{^3\mathrm{H}}(x, Q^2) = \int_x^3 dz \frac{1}{3}\left[f_p^{^3\mathrm{H}}(z, Q^2)F_2^p\left(\frac{x}{z}, Q^2\right) + 2f_n^{^3\mathrm{H}}(z, Q^2)F_2^n\left(\frac{x}{z}, Q^2\right)\right] \tag{2.22}$$

$$= \int_x^3 dz \frac{1}{3}\left[f_n^{^3\mathrm{He(no\ Coul)}}(z, Q^2)F_2^p\left(\frac{x}{z}, Q^2\right) + 2f_p^{^3\mathrm{He(no\ Coul)}}(z, Q^2)F_2^n\left(\frac{x}{z}, Q^2\right)\right]. \tag{2.23}$$

Next we compare the above considerations with some results. Figures 5(a) and 5(b) show for $Q^2 = 2.5$ and 7.5 GeV^2, respectively, the distribution functions $f_{p,n}^{^3\mathrm{He}}(x, Q^2)$, Eq. (2.8). The solid, dashed, and dotted lines correspond to interactions B2(0), B2(0 + 1), and B2 + B3(0 + 1), where the numbers indicate the order of terms retained. Since FSI terms are retained, results for B2(0) serve only to indicate the relative importance of the two terms. Figure 5(c) compares $f_p^{A=3,I_3}(x, Q^2 = 5)$, Eq. (2.20), to which we shall return in Sec. II C.

At this point we need to mention that, for any Q^2, the norm of the lowest-order term $\mathcal{N}_x = \int_0^3 dx\, f_{p,n}^{A=3;(0)}(x, Q^2) = 1$. A more extensive discussion can be found in the Appendix.

These $A = 3$ distribution functions follow a standard pattern for all light A [33]: for increasing Q^2 the peak of $f^{A=3}$ increases and the width shrinks correspondingly. For instance, for Q^2 increasing from 2.5 to 10.0 GeV^2, the B2 p peaks increase from 4.041 to 5.394 and the n peaks from 3.483 to 4.648. Peak values for B2 + B3 are ≈4% lower than for B2 and are correspondingly wider. Also, for the same Q^2 these are intermediate between the values for ^{2}H and ^{4}He.

Figure 6 displays computed SFs $F_2^{^3\mathrm{He}}$ for fixed $\theta = 40^\circ$ and variable $Q^2(x, \theta)$, using Eqs. (2.21) with B2 or B2 + B3 interactions. The results for those are practically indistinguishable from and quite close to the SF sextracted using data and $R \approx 0.36/Q^2$ for the ratio of inclusive scattering of virtual longitudinal and transverse photons. The lower curve in Fig. 6 is for $F_2^{^3\mathrm{H}}$, Eq. (2.23): with no data, there is no extracted parallel. One notices, however, the sizable difference between predictions for the members of the isodoublet.

Figures 7(a) and 7(b) present on a linear scale data and computed inclusive cross sections on ^{3}He for $\theta = 18^\circ, 40^\circ$. Cross sections for $\theta = 40^\circ$ for ^{3}He using either B2 or B2 + B3 interactions are in good agreement with data. This outcome should be compared with the same for other targets shown in Fig. 1 on a logarithmic scale, and the same for the QE range in Fig. 2 on a linear scale. The rather poor fit for ^{3}He, $\theta = 18^\circ$ is in striking contrast with the fit for $\theta = 40^\circ$, in spite of the use of the same underlying analysis. We cannot forward any theoretical explanation.

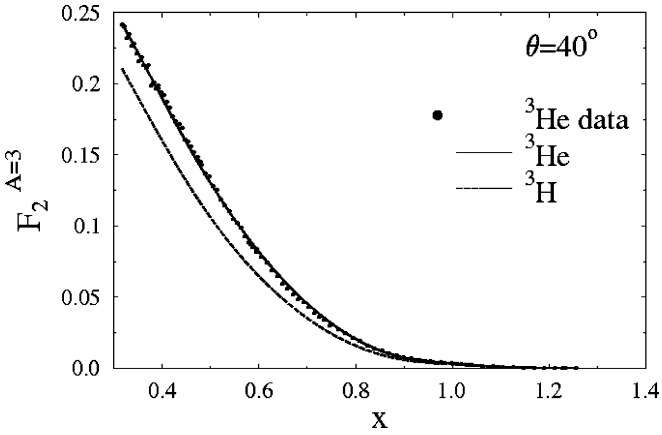

FIG. 6. Computed and extracted $F_2^{^3\mathrm{He}}(\theta = 40^\circ)$ for B2 + B3 interactions. Lower curve is for $F_2^{^3\mathrm{H}}(\theta = 40^\circ)$.

C. EMC ratios

At least some difficulties in understanding the new total cross section data may be caused by unknown systematic errors, the size of which can only be estimated. Since ^{2}H is among the targets, some of those errors may cancel in the EMC ratios $\mu^A = F_2^A/F_2^{^2\mathrm{H}}$. For that reason alone is it of interest to compare measured with computed ratios.

The new EMC data are for a few discrete θ and thus not for fixed Q^2. Although the resulting Q^2 dependence is mild, it should be borne in mind that, for instance, for the chosen angle $\theta = 40^\circ$, data on the released or measured additional x ranges cover $2.80 \lesssim Q^2\ (\mathrm{GeV}^2) \lesssim 6.12$, which is not an insignificant variation in $\mu(Q^2)$. The published data are for $x_{\min}^{\mathrm{data}} \leqslant x \lesssim 0.9$, $x_{\min}^{\mathrm{data}} \approx 0.35$ [6], and correspond to what occasionally is called the "classical" EMC range. Within that range the variation of Q^2 has less spread and causes less than 1% variations in EMC ratios.

Measured $\mu^{^4\mathrm{He}}$ and $\mu^{^{12}\mathrm{C}}$ [6] have a somewhat smaller slope than older data, in particular for ^{4}He (see, for instance, Ref. [34]). In Figs. 8(a) and 8(b) we compare the new data with previously computed GRS results for $Q^2 = 3.5, 5.0\,\mathrm{GeV}^2$ [33] and for additional Q^2, close to the above-mentioned binned ones. The agreement is reasonable.

We also mention a prediction, based on the Q^2 independence of $F_2^{p,^2\mathrm{H}}(x \approx 0.20, Q^2)$ [19]. Since all distribution functions f^A are negligible for $x \lesssim 0.4$, one may replace the lower integration limit in the expression (2.1) for F_2^A by 0. Then, using unitarity, that is, $\mathcal{N}[f^A] \approx \mathcal{N}[f^{A;(0)}] = 1$, all $F_2^A(x \approx 0.20, Q^2)$ computed by Eq. (1.3) are predicted to be roughly independent of Q^2 as well as of A. Consequently, EMC ratios $\mu^A(x, Q^2)$ ought to intercept the x axis at a value $\mu^A(x \approx 0.2, Q^2) \approx 1$ [33]. This holds when only one distribution function is involved, that is, for $I = 0$ nuclei, or when an averaged f^A is sufficiently accurate in all other cases.

The actual crossover $\mu^{A,^2\mathrm{H}} = 1$ for most nuclei (and for several $\mu^{A,A'}$) is $x_{\mathrm{co}} \approx (0.2\text{–}0.3)$, whereas the intercept of the $I = 0$ ND seems to occur for somewhat higher $x \approx 0.33$ [6].

Again we discuss separately the case of the $A = 3$ isodoublet with different f_p and f_n. In the previous section we presented results for computed SFs and cross sections for the $A = 3$ doublet, using various input options. For completeness we add for ^{3}He the "standard" extraction of its SF from cross section data. Although this exists for several options, we report only on computed results for B2 + B3 interactions and calculated EMC ratios as $F_2^A/F_2^{(^2)\mathrm{H}}$ or $\sigma^A/\sigma^{(^2)\mathrm{H}}$.

As discussed above, we need option (i) in Sec. II B for ^{3}He with no V_{Coul}, in order to compute the the SF for the isopartner ^{3}H. Data are much desired [35,36], but it will take years before those will become available and can be confronted with $F_k^{^3\mathrm{H}}$ calculated, for instance, from Eq. (2.23) (cf. also [16,36,37]).

In Fig. 9(a) we show three curves for $\mu^{A=3;F_2}(\theta = 40^\circ)$ from ratios of SFs. The top and bottom ones are for ^{3}He and ^{3}H, while the middle one, for half their sum, is the computed $I = 0$ part of either member of the isodoublet. One notices the widely different behavior of the two ratios: In the classical EMC region, $\mu^{^3\mathrm{He}} > 1$, has a positive x slope and shows no minimum for medium x. In contrast $\mu^{^3\mathrm{H}} < 1$, has a negative x slope and an unexpectedly deep minimum for $x \approx 0.7$. The isosinglet part has positive slope, crosses 1 at $x \approx 0.8$, and has no visible minimum.

Figure 9(b) shows $\mu^{A=3;\sigma}(\theta = 40^\circ)$, but now as ratios of cross sections, which are seen to differ from the results in Fig. 9(a): $\mu^{^3\mathrm{He}} \gtrsim 1$ for $x \lesssim 0.85$ and has a maximum for $x \approx 0.75$. In contrast $\mu^{^3\mathrm{H}} < 1$, has negative x-slope and shows a shallow minimum for $x \approx (0.6\text{–}0.7)$. Essentially the same holds for the isoscalar part, but the ^{3}He part there pushes the $I = 0$ part an amount ≈0.1 upward on the μ scale.

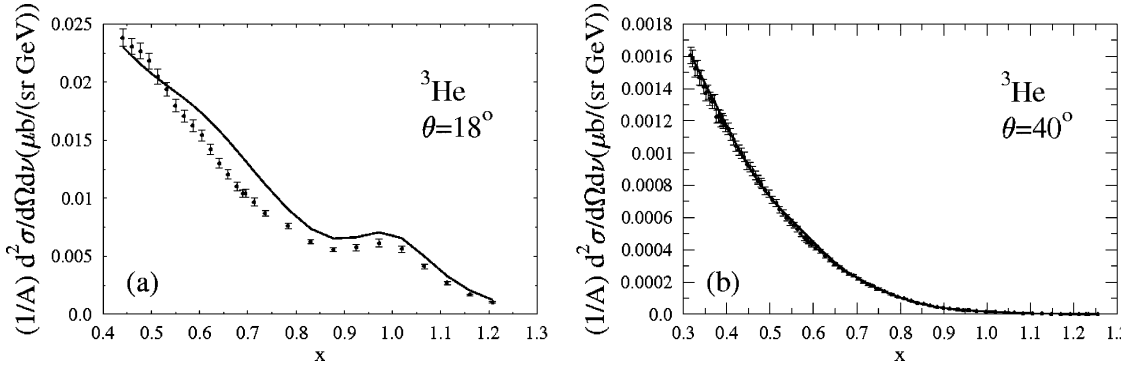

FIG. 7. (a),(b) Computed total inclusive cross sections on ^{3}He for $\theta = 18^\circ, 40^\circ$. Data with error bars are from [7].

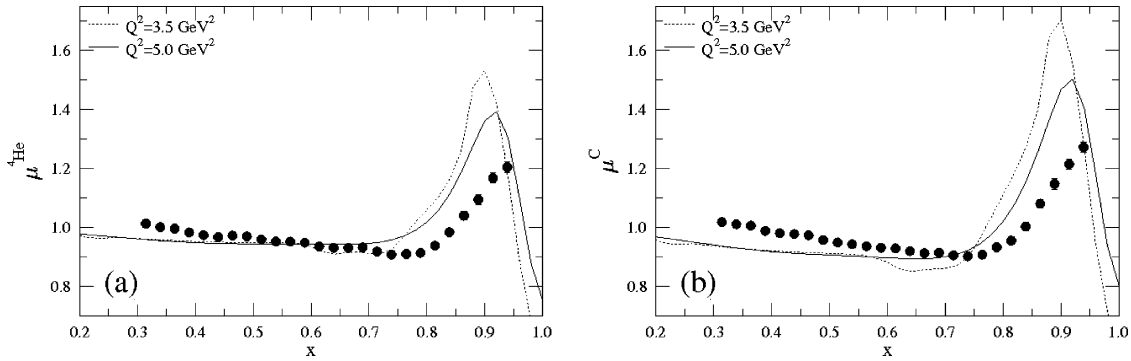

FIG. 8. EMC data $\mu^{^4\mathrm{He}}(x \lesssim 1.0, \theta = 40^\circ)$ (a) and same for C (b) [6], and computed results for fixed $Q^2 = 3.5, 5.0\ \mathrm{GeV}^2$.

The empty circles in Fig. 9(b) are the data of Seely *et al*. [6] for ^{3}He from ratios of bona fide cross sections, although they are called by the authors "raw data" [empty circles in Fig. 9(b)]. Comparison with the upper drawn curve shows rough agreement. In contrast to a genuine calculation of the isoscalar part (dashed curve), the above-mentioned authors modify the above "raw data" in a standard fashion, which does not require information on ^{3}H. This leads to a fictitious $I = 0$ nucleus with $N = Z = A/2$ amounting to

$$f_{p,n}^{A(Z,N)} \approx f^A(Z = N) \approx f^A\left(\frac{A}{2}, \frac{A}{2}\right). \qquad (2.24)$$

This is considered to be a model for the EMC ratio of an even nucleus with $I \neq 0$ and instructive, even for interpolation to $A = 3$ [6].

The results hardly change when θ runs over the entire measured range, and this holds in particular for their I_3 dependence. One should keep in mind that the EMC effect, small in any case, is the deviation from 1 of the ratio of small numbers. That effect becomes even smaller when going to the lightest nuclei, increasing its precarious sensitivity. In this relation we recall the I spin dependence in Fig. 5(c) of the p distribution function in the isodoublet, assuming isospin symmetry after correcting for V_{Coul}. The two may well be related.

III. THE MAGNETIC FF OF THE NEUTRON AND CLAS DATA

In the previous sections, we encountered clear discrepancies between the NE components in the ND and OD results in the QE regions of total inclusive cross sections. Their description requires the dominant reduced n magnetic FF $\alpha_n = G_n^M/[\mu_n G_d]$ in the QE region. In the following we recall attempts to isolate and to extract α_n.

At this point we remark that on the one hand the entities G_M^n (and F_k^n considered in the following section) are needed to determine the total SFs F_A and the inclusive (reduced) cross sections σ^A. However, one wishes to extract those from QE data. The procedure is to use some starting values in the input, compare the output until self-consistency is reached, and compare the outcome with the starting values.

The expressions (1.4) and (1.5) locate two functions with pronounced peaks for $x \approx 1$. Those are the NE parts of the reduced cross section $K^{A;\mathrm{NE}}(x, Q^2; E, x)$, Eqs. (1.1) and (2.11), and the linking distribution function $f^A(x, Q^2)$, functions of five and three variables, respectively.

In appears that their ratio $K^{A;\mathrm{NE}}/f^A$ is primarily a function of Q^2 with only weak additional dependence on x, θ, E, and A. As suggested in the past, we turn this into a criterion, to be satisfied by candidates x_l for extraction.

For sufficiently accurate and smooth data one tries to locate a *continuous* x range in the QE region for which the above

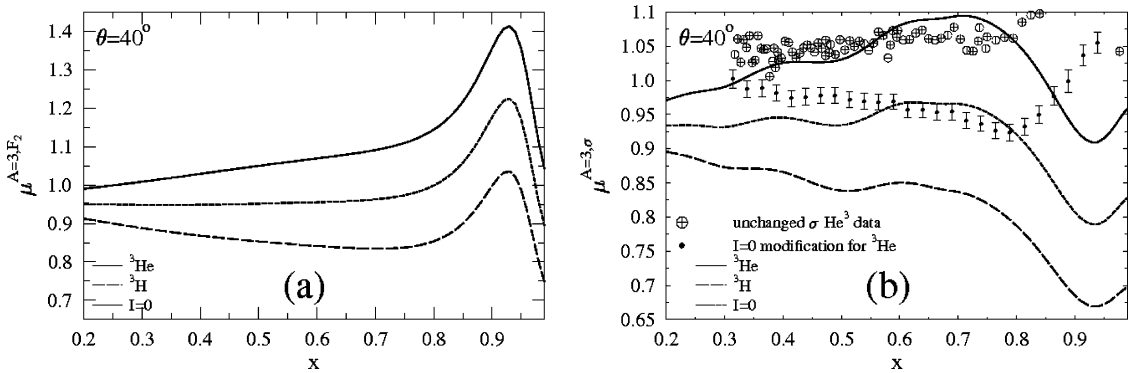

FIG. 9. $\mu^{A=3;F_2}(\theta = 40^\circ)$ from ratios of SFs F_2 (a) for ^{3}He and ^{3}H (solid line and long dashes), and from ratios of cross sections (b). Short dashes as for the isoscalar components. In (b) empty and full circles are direct data for ^{3}He and manipulated ones for a fictitious isoscalar $A = 3$ nucleus, respectively [6].

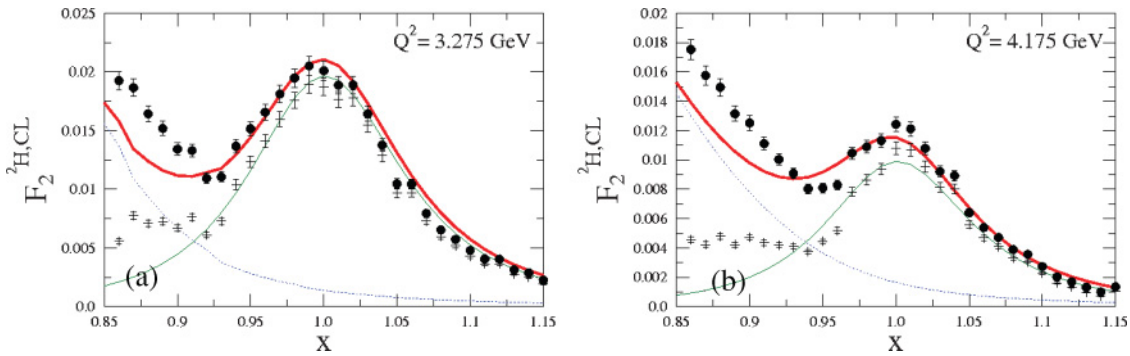

FIG. 10. (Color online) Data with error bars for SF $F_2^{^2\mathrm{H}}(x, Q^2)$ from CL data (filled circles) [13]. (a) and (b) are for $Q^2 = 3.275$ and 4.175 GeV^2. Legend as in Fig. 1.

ratio does not vary by more than a prescribed amount, say, 10%. If such a range is available, one finds [cf. Eq. (4.3) in Ref. [25]]

$$\alpha_n|\mu_n| = \left(\frac{2MK^{A,\mathrm{NE}}/[vfG_d] - B^2/\eta}{1+\tan^2(\theta/2)/v} - (\alpha_p\mu_p)^2\right)^{1/2}, \tag{3.1}$$

where the Q dependence is implicit. Here, G_d is the standard dipole FF, $v = x^2/2(1+\eta)$, $\beta_N = G_E^N/G_d$, $\alpha_N = G_M^N/[\mu_N G_d]$, and $B^2 = \beta_p^2 + \beta_n^2$. Equation (3.1) generalizes for $f_n \neq f_p$ as

$$\frac{N}{A} f_n[\alpha_n\mu_n]^2 + \frac{Z}{A} f_p[\alpha_p\mu_p]^2 = \frac{MK^{A;\mathrm{NE}}/vG_d^2 - \left[Zf_p\beta_p^2/(A\eta) + Nf_n\beta_n^2\right]}{1+\tan^2(\theta/2)/v}. \tag{3.2}$$

$\alpha_n(Q^2)$ is of course only a function of Q^2, but because of imperfect data and theory the algorithm produces an inherent, weak dependence on the chosen points x. Whereas there is no physical meaning to individual x-dependent results, it is natural to define the extracted $\alpha_n(Q^2) \equiv \langle\alpha_n(Q^2)\rangle = \langle\alpha_n(x;Q^2)\rangle_x$ as an appropriate average over the selected x range. For all previously investigated OD the above criterion is met for a suitable number of continuous x points (see the table in Ref. [25]). As to ND, only for $^2\mathrm{H}(\theta \lesssim 32^\circ)$ could we find two or three such points. However, those points appear to produce through Eq. (3.1) a value for α_n far from the OD results for similar Q^2.

Like the material discussed in Secs. I and II, this also indicates that in the QE region the new and old data sets do not match. We emphasize two points, relevant for OD. One is the very applicability of the suggested analysis for OD data, in contrast to the same for ND. Moreover, *different* sets with approximately the same Q^2 produce essentially the same $\alpha_n(Q^2)$, providing evidence for internal consistency [25].

As a last resource we invoke the CLAS Collaboration data on $F_2^{^2\mathrm{H}}$, which have not been subjected to a similar analysis before. These are available for a dense net of Q^2 ($\Delta Q^2 = 0.05$ GeV^2), which for each Q^2 cover a wide and dense x range ($\Delta x = 0.009$) [13]. We apply the above-mentioned criterion regarding the K/f ratio to those data and look for continuous x ranges around the QEP for $\theta = 18^\circ, 22^\circ, 26^\circ$, and 32°, which approximately correspond to $Q^2 \approx 2.50,\ 3.275,\ 4.175$, and 5.175 GeV^2. Regrettably, CL data do not extend to larger Q^2, covering $\theta = 40^\circ$ and 50° in ND.

Further, for the CL data one cannot, strictly speaking, apply the above criterion for a continuous x range in every data set. However, a representative number of candidate x points remains after removal of at most one or two points per set, for which the observed scatter of neighboring points exceeds 10%. The extracted $\langle\alpha_n(Q^2)\rangle$ appears to match the OD results.

We first show in Figs. 10(a) and 10(b), in much the same way as in Figs. 1 and 2, the components $\mathrm{NI}^{^2\mathrm{H,calc}}$, $\mathrm{NE}^{^2\mathrm{H,FF}}$, and $\mathrm{NE}^{^2\mathrm{H,extr}}$ for two of the above four data sets with $Q^2 = 3.275$ and 4.175 GeV^2. Whereas this depiction is clearly useful around the QEP, some disagreement between the two NE representations grows toward the inelastic wing of the QE peak. It is similar in size and shape as for OD [25], but not anywhere as disastrous as for the above-mentioned ND.

In Table I we entered $F_2^{^2\mathrm{H}}$ for the above four angles over a range of x and correspondingly varying Q^2 values. In the last three columns we compare (i) the values *extracted* from the ND, assuming the standard transverse to longitudinal ratio $R \approx 0.36/Q^2$; (ii) the same *computed* from Eq. (1.3); and (iii) the CL data for $F_2^{^2\mathrm{H}}$. Differences seem largest around the QEP and occasionally switch sign. No similarly large aberrations are apparent in the analysis of linear plots of the OD.

Table II contains the reduced magnetic FF α_n^{CL} from the CLAS data, Q^2, the range, and the number of chosen x points. Column 4 states the averaged $\langle\alpha_n(Q^2)\rangle$ with the error of the mean. To the statistical errors we added in quadrature estimated 2% systematic ones.

In Fig. 11 we assemble $\alpha_n(Q^2)$ as extracted from the OD and CL data for four values $Q^2 = 2.501,\ 3.275,\ 4.175$, and 5.175 GeV^2, together with a previously extracted parametrization, Eq. (5.4), Ref. [25]. For completeness we added to the above all α_n with $Q^2 \geqslant 2.5$ GeV^2 [25], extracted from OD. The CL and old data sets produce essentially the same results and trend.

Figure 11 displays $\langle\alpha_n(Q^2)\rangle$, extracted from the CL data for closely spaced Q^2 around the four values above. While these vary by (0.5–1.0)% in going from one Q^2 bin to a neighboring one, entries within each bin show larger variations within a standard deviation of $\langle\alpha_n(Q^2)\rangle$.

In Fig. 11 we also entered $\alpha_n(Q^2)$, recently extracted from the cross section ratio $^2\mathrm{H}(e,e'n)p/^2\mathrm{H}(e,e'p)n$ for

TABLE I. Values of $F_2^{^2\mathrm{H}}(x, Q^2)$, extracted and computed from ND, and the same from CL [44] for a chosen x range (columns 1). Column 2 gives $Q^2(x, \theta)$ for that x range and $\theta = 18^\circ, 22^\circ$, ($\theta = 32^\circ, 40^\circ$). Columns 3, 4, and 5 are for ND $F_2^{^2\mathrm{H,extr}}$, $F_2^{^2\mathrm{H,calc}}$, and $F_2^{^2\mathrm{H,CL}}$ for given x and the above two pairs of angles. Empty entries correspond to missing data.

x	$Q^2(18^\circ)$	$F_2^{^2\mathrm{H};R}(18^\circ)$	$F_2^{^2\mathrm{H;calc}}(18^\circ)$	$F_2^{^2\mathrm{H;CL}}(18^\circ)$	$Q^2(26^\circ)$	$F_2^{^2\mathrm{H};R}(26^\circ)$	$F_2^{^2\mathrm{H;calc}}(26^\circ)$	$F_2^{^2\mathrm{H;CL}}(26^\circ)$
0.5	2.03	0.153	0.154	0.156				
0.6	2.17	0.0985	0.102	0.105	3.31	0.0884	0.0910	0.0094
0.7	2.28	0.0555	0.0530	0.0559	3.56	0.0522	0.0542	0.0556
0.8	2.36	0.0387	0.0333	0.0464	3.79	0.0241	0.0238	0.0272
0.9	2.43	0.0225	0.0200	0.0171	3.98	0.0109	0.0108	0.0126
1.0	2.51	0.0344	0.0369	0.0406	4.15	0.0110	0.0123	0.0129
1.1	2.56	0.0086	0.0112	0.0097	4.29	0.0022	0.0026	0.0022
x	$Q^2(32^\circ)$	$F_2^{^2\mathrm{H};R}(32^\circ)$	$F_2^{^2\mathrm{H;calc}}(32^\circ)$	$F_2^{^2\mathrm{H;CL}}(32^\circ)$	$Q^2(40^\circ)$	$F_2^{^2\mathrm{H};R}(40^\circ)$	$F_2^{^2\mathrm{H;calc}}(40^\circ)$	$F_2^{^2\mathrm{H;CL}}(40^\circ)$
0.4					3.37	0.184	0.174	0.187
0.5					4.02	0.125	0.124	0.128
0.6	3.95	0.0801	0.0810	0.0775	4.59	0.0740	0.0750	0.0785
0.7	4.33	0.0471	0.0480	0.0450	5.09	0.0404	0.0415	0.0442
0.8	4.66	0.0204	0.0210	0.0225	5.58	0.0186	0.0182	0.0212
0.9	4.95	0.0089	0.0083	0.0096	5.99	0.0065	0.0058	0.0088
1.0	5.23	0.0055	0.0064	0.0053	6.39	0.0034	0.0035	0.0035

$Q^2 = (1.0$–$4.8)$ GeV^2. Each FF point has been measured with an error less than 3%, but again, for $Q^2 \gtrsim 2.5$ GeV^2, and most obviously for $Q^2 \gtrsim 3.4$ GeV^2, the scatter between adjacent points is often far larger. The results (Fig. 5 in Ref. [38]) are reproduced in Fig. 11 together with those of Ref. [39].

We conclude this section by mentioning a recent calculation of space- and timelike nucleon FFs using a light-front framework [40]. Whereas spacelike p FFs are well reproduced, the computed α_n shows a maximum, which diminishes toward 0 for large Q^2. That result disagrees considerably with those displayed in Fig. 11, where the almost coincident extractions from the CLAS Collaboration data and the OD produce a continuous decrease, which persists out to $Q^2 \approx 10$ GeV^2.

TABLE II. α_n extracted from inclusive scattering on ^{2}H [44]. Column 1 gives the group of values of Q^2, around $Q^2 = 2.50$, 3.34, 4.15, and 5.24 GeV^2, which correspond to the values $Q^2(\theta = 18^\circ, 22^\circ, 26^\circ, 32^\circ; x = 1)$ Columns 2 and 3 are the x range of points around the QEP and the number of selected points n. The last column gives the average over the given x range of $\langle\alpha_n(Q)\rangle$, the reduced magnetic FF of the n, and the error of the mean.

Q^2 (GeV)^2	x interval	n	$\langle\alpha_n\rangle \pm \delta\alpha_n$
2.425	0.9235–1.0405	12	1.0005 ± 0.0334
2.475	0.9235–1.0405	12	0.9837 ± 0.0310
2.525	0.9235–1.0315	12	1.0020 ± 0.0294
2.575	0.9235–1.0315	10	1.0488 ± 0.0324
3.275	0.9415–1.0225	9	0.9752 ± 0.0344
3.325	0.9595–1.0225	6	0.9917 ± 0.0475
3.375	0.9325–1.0225	7	0.9720 ± 0.0448
4.075	0.9685–1.0675	9	0.9822 ± 0.0430
4.125	0.9775–1.0855	9	0.9614 ± 0.0497
4.175	0.9685–1.0855	11	0.9415 ± 0.0354
4.225	0.9775–1.0765	8	0.9804 ± 0.0309
5.075	0.9865–1.0675	6	0.9237 ± 0.0593
5.175	0.9685–1.0585	6	0.9001 ± 0.0350
5.275	0.9865–1.0765	5	0.8753 ± 0.0625
5.375	0.9685–1.1035	7	0.9145 ± 0.0378

IV. EXTRACTION OF F_2^n FROM CLAS DATA

The neutron SF F_2^n complements information from F_2^p on the valence quark distribution functions u_v and d_v in the N: Its knowledge is a minimal requirement to disentangle the two distributions. Lacking reliable information on F_2^n, one occasionally invokes the SU(6) result $[F_2^n/F_2^p]_{\mathrm{SU(6)}} = 3/5$, which amounts to $u_v = 2d_v$. Alternatively, one uses the "primitive" choice $F_2^n = 2F_2^{^2\mathrm{H}} - F_2^p$, the reliability of which is restricted to $x \lesssim 0.35$.

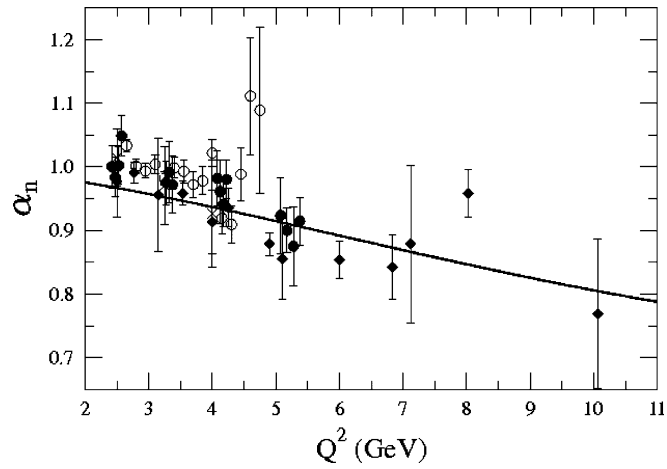

FIG. 11. Averaged reduced neutron magnetic α_n (Table II). On the curve for OD filled circles are results from CL (Sec. III), crosses from Lung [39], and diamonds for all results from Table I in Ref. [25] for $Q^2 \geqslant 2.5$ GeV^2. Open circles are from a $^2\mathrm{H}(e, e'n)p/^2\mathrm{H}(e, e'p)n$ experiment (Fig. 4, Ref. [38]).

It is clearly desirable to have empirical information on F_2^n along with $F_2^{p,{}^2\mathrm{H}}$ for $x \gtrsim 0.3$ in order to determine N parton distributions. With no free n target available, one has to extract F_2^n from bound neutrons. The preferred target has been ^{2}H, for which the nuclear information is simplest and most accurately known, but the literature also describes the extraction of F_2^n from future precision data on the SFs for ^{3}He and ^{3}H (e.g., Refs. [16,36,37]) and heavier targets [20].

Several extraction methods have been proposed in the past. For instance, an approximate inversion of Eq. (1.3) requires reliable data points on F_2^A, and preferably for several targets. Previously we found that data were barely sufficient to extract F_2^n from a single binned $\bar{Q}^2 = (3.5\text{–}4.0)\ \mathrm{GeV}^2$. We summarize the steps of the procedure followed [20], which will also be exploited here.

(i) Assume $C(x, Q^2) \equiv F_k^n(x, Q^2)/F_k^p(x, Q^2)$ to be independent of k.

(ii) Assume $C(0) = 1$, as implied by a finite Gottfried sum $\int_0^1 dx[F_2^p(x, Q)2 - F_2^n(x, Q^2)]/x$.

(iii) Assume the validity for $x \lesssim 0.30\text{–}0.35$ of the "primitive" approximation $F_2^{^2\mathrm{H}} = [F_2^p + F_2^n]/2$, that is, $C = 2F_2^{^2\mathrm{H}}/F_2^p - 1$. In practice we use $p,{}^2$H data for two points, chosen to be $x = 0.15, 0.25$. The information (ii) and (iii) mainly determines the decrease of $C(x, Q^2)$ from 1 for x increasing from 0 to about $x \lesssim 0.6$.

(iv) A last step is a chosen parametrization for $C(x, Q^2) = \sum_{k\geqslant 0} d_k(Q^2)(1-x)^k$. For $k = 3$, (ii) and (iii) leave one parameter to be determined, and the natural candidate is $C(1, Q^2) = d_0(Q^2) = 1 - \sum_{k\geqslant 1} d_k(Q^2)$.

A remark on $C(1)$ is in order here. Both SFs $F_2^{p,n}(x, Q^2)$ vanish for finite Q^2 beyond the lowest inelastic pion production threshold at $x_{\pi\,\mathrm{thr}}(Q^2) \approx 1/\left[2M\mu_\pi/Q^2 + 1\right]$, and the NI continuum is therefore isolated from the elastic peak at $x = 1$. The SFs of the latter are given by Eqs. (1.4) and (1.5) in terms of FFs. Neglecting G_E^n, one finds (typos in Ref. [20] have been corrected below)

$$\lim_{x\to 1} C^{\mathrm{FF}}(x, Q^2) = \left(\frac{\mu_n \alpha_n(Q^2)}{\mu_p \alpha_p(Q^2)}\right)^2 \left[1 + \frac{4M^2}{Q^2}\left(\frac{\gamma(Q^2)}{\mu_p}\right)^2\right]^{-1} \tag{4.1}$$

with

$$\gamma(Q^2) = \frac{\mu_p G_E^p(Q^2)}{G_M^p(Q^2)}, \quad \frac{\alpha_n(Q^2)}{\alpha_p(Q^2)} = \frac{G_M^n(Q^2)/\mu_n}{G_M^p(Q^2)/\mu_p}. \tag{4.2}$$

C was then determined by a least-squares fit for the sum $\sum_{x_m}^{x_M}$ and not point by point in x. Naturally, any parametrization of C, and in particular (iv) above, ascribes values to C in the unphysical region $1 \gtrsim x \gtrsim x_r(Q^2)$.

The extracted parameter $d_0(Q^2) = C(1, Q^2)$ fairly rapidly reaches a plateau for increasing Q^2. Since $\lim_{x\to 1} F_2^{p,n;\mathrm{NI}}(x, Q^2) = 0$, it is not surprising to find that values for $C(x \lesssim 1, Q^2)$ on the plateau, that is, the extrapolation from the adjacent nonphysical region to the largest $x > x_{\mathrm{thr}}$, and ultimately to $x = 1$, depends sensitively on the upper limit taken in the x sum above. Thus, for $x_M = 0.75$ and increasing Q^2 in the range $4 \lesssim Q^2\ (\mathrm{GeV}^2) \lesssim 10$, the extracted $C(1, Q^2)$ decreases from 0.38 to 0.27, while $C^{\mathrm{FF}}(1, Q^2)$, Eq. (1.5), barely decreases form 0.38 to 0.37. For a slightly larger $x_M = 0.80$, $C(1, Q^2)$ decreases from 0.34 to 0.25 over a much narrower Q^2 interval than for $x_M = 0.75$.

The procedure has been checked by a recalculation of $F_2^{^2\mathrm{H}}$, using the extracted F_2^n in Eq. (1.3): The initial $F_2^{^2\mathrm{H}}$ appears accurately reproduced. Figures 12(a) and 12(b) show $C^{^2\mathrm{H}}(x, Q^2)$ as well as $F_2^{p,n}$ for $Q^2 = 2.5, 7.5\ \mathrm{GeV}^2$ and $x_M = 0.75$. Although there is an influence on C for $x = 1$, one can only barely distinguish between $C(x \lesssim 0.85, Q^2)$, computed for either $x_M = 0.75$ or 0.80.

Alternative attempts have been made in the past in order to obtain F_2^n, all of which use a ^{2}H target. One, for instance, replaces the distribution function $f^{\mathrm{PN},{}^2\mathrm{H}}$ in Eq. (1.3) by a momentum distribution or some generalization of the latter, and uses it to "smear" nucleon SFs [41]. From the difference $\langle F_2^n\rangle_f = F_2^{^2\mathrm{H}} - \langle F_2^p\rangle_f$, featuring folded or smeared SFs, the "bare" F_2^n has to be deconvoluted. An iteration method has recently been tested on the Mainz Data Collection (MAID) parametrization for F_2^N [42]. The reported success may in part be due to the fact that the procedure, as well as the parametrized input, imply the use of a smooth average. Application to real data with non-negligible fluctuations may well run into the difficulties discussed above. We also mention an extraction of F_2^n from essentially the impulse approximation for $f^{PN;{}^2\mathrm{H}}$, using

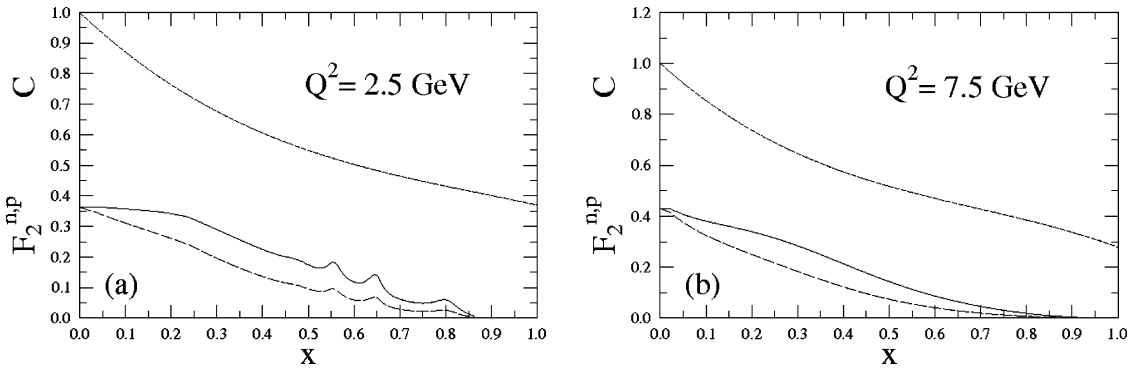

FIG. 12. Extracted $C(x, Q^2)$ for $x_M = 0.75$ (short dashes) and $F_2^{p,n}(x, Q^2 = 2.5\ \mathrm{GeV}^2)$ (solid and dashed curves). (a) and (b) are for $Q^2 = 2.5$ and $7.5\ \mathrm{GeV}^2$.

the parameterized ratio $F_2^{^2\mathrm{H}}/F_2^p$, F_2^p and the ^{2}H wave function [43]. Most published $C(x, Q^2)$ follow the same trend for $x \lesssim 0.75$ and are primarily distinguished by the extrapolated $C(x = 1)$.

Finally, we recall the extraction of the leading twist moments of $F_2^{p,^2\mathrm{H}}$ from the CL data. By means of a convolution like Eq. (1.3), those are subsequently used to construct parallel twist moments for n [44]. This analysis enables a proper definition of averaged α_n. No inversion leading to $F_2^n(x, Q^2)$ has been reported there.

V. DISCUSSION AND CONCLUSIONS

It has been our goal to describe the Jlab experiments E103-102 and E02-90 on inclusive electron scattering from various targets, specifically for total cross sections and EMC ratios [6]. Subsequently we tried to extract from those the (reduced) magnetic FF $\alpha_n(Q^2)$ and the SF $F_2^n(x, Q^2)$ of a neutron bound in a nucleus. These are, respectively, the dominant part of the NE component in the QE region and a vital component of the inelastic part of the total cross section.

For the ND, we also used the GRS approach, which has previously been applied to all older experimental information [25]. Only minor changes in theoretical elements have been applied since; for instance, the inclusion of two-photon exchange corrections to the electric FF of the proton.

We first mention that the most reliable results from the OD were obtained in the DIS region, where inclusive scattering is entirely inelastic. For the smallest x we found agreement with data, not rarely to within (2–3)%. For increasing x, strongly decreasing NI parts have to be accurately known in order to isolate with precision the NE parts dominating the QE region [25]. For medium x between the "elastic tails" of (pseudo)resonances and their peaks, disagreements appear, which are reflected in the difference between the extracted and computed NE components.

A possible cause of the above disagreements could be uncertainties in the proton SF. We checked that a mild relative change of NI, which grows to $\approx 15\%$ in the NE/NI interference region, and again decreases toward the higher NI resonances, brings about agreement. Such an uncertainty in the parametrization of F_2^p in the required Q^2 region apparently hardly affects the quality of the extracted F_2^p [18].

Next we considered the extraction of the n magnetic FF from data in the QE region. We utilized a previously formulated criterion for such an extraction, which requires a continuous set of eligible x points for which the ratio of the x-dependent reduced total cross section and the computed distribution function falls within predetermined limits. The criterion could be satisfied for all old data sets, which moreover showed consistency: The same α_n resulted from different data sets with overlapping Q^2 values.

From new precision data one expects agreement of at least the same quality. Using exactly the same program as before, we analyzed all measured data, of which only a fraction has been published. The major results are as follows.

(i) Even in the DIS region, the best agreement is not better than (5–6)%, and not infrequently of both signs.
(ii) Measured EMC ratios for light isoscalar nuclei approximately agree with previous data and calculations.
(iii) The same seems to hold for model-independent features for $x \approx 0.20$.
(iv) It is virtually impossible in any QE region to satisfy our criterion on candidate x points for the extraction of α_n. As a rule NE values obtained as the difference between data and computed NI components do not match NE values computed from FFs anywhere. The required changes in NI parts leading to a match by far exceed the moderate ones described in Ref. [25].

At this point we mention a suggestion to integrate the QE peak over some x interval and to extract α_n in this way [45]. We doubt whether the suggested procedure can produce reliable averages for locally varying relative systematic errors.

The only alternative material that we could use in the above analysis are the CLAS Collaboration data on ^{2}H [13], which have apparently not been analyzed before. From those we could extract both α_n and F_2^n and the former essentially matched older results.

Particular attention has been paid to the $A = 3$ isodoublet. Many years after the first data were taken, the new experiments contain information on ^{3}He, while theory has also much advanced. Most significantly there are available results on exact calculations of the $A = 3$ single p, n spectral functions for several NN interactions. Those underlie the calculation of the dominant contribution of the separate p, n distribution functions in both ^{3}He and ^{3}H, with the latter using charge symmetry when V_{Coul} is neglected. We thus calculated for the GRS theory the SFs of ^{3}He and ^{3}H and inclusive cross sections.

We started with σ^3He for all six measured angles and found only crude agreement for the lower angles, but good correspondence for the largest ones, in particular for $\theta = 40^\circ$. Since we used one and the same theory for all, theory cannot be blamed for the striking dissimilarity.

Next we computed the two EMC ratios $\mu^{A=3}(\theta = 40^\circ)$ and their isoscalar mean, once as ratios of F_2 and then alternatively from cross sections. The data for ^{3}He in the classical EMC region hover around 1 and do not show a minimum around $x \approx 0.5$–0.6. About the same is predicted by theory.

The results are quite different for ^{3}H, for which theory predicts a more standard behavior with $\mu \lesssim 1$ and a shallow minimum. Lack of data prevent a comparison with the theoretical outcome. However, one may discuss the computed isoscalar part, which resembles a standard EMC ratio with a growing negative slope for decreasing A from $A = 12$ down to ^{2}H. The slope of the isovector part $\mu^{A=3;I=0}(\theta = 40^\circ)$ lies between those for ^{4}He and ^{2}H.

As to raw data, in a standard procedure one estimates μ^A for nuclei with a nucleon excess, replacing that EMC ratio by one for a fictitious isobar with $Z = N = A/2$. The published data

for the isoscalar part of ^{3}He agree quite well with the computed ones. It should be clear that theory computes a real result, while the data relate to a somewhat dubious extrapolation to the lowest $I \neq 0$ nucleus.

We return to the enigmatic outcome for several nonisolated ND. Since the same tools were used before, the most extreme conclusion could be incompatibility of the old and new sets. A milder judgment blames systematic errors. We included those as a fixed estimated percentage, but it is clear from the scatter of neighboring accurate points that more than average systematic errors are required in order to bring about agreement.

We also emphasize that all cross section data sets are reported to have normalization uncertainties in the range (2.2–2.7)% [7]. Those may cause some of the observed discrepancies, but not those between inclusive cross sections on ^{3}He for $\theta = 18^\circ$ and 40° in similar data sets.

One may raise the question of whether a fundamental parton description might significantly modify results based on the hadronic representation used. Only recently has attention been redrawn to two old communications regarding a QCD treatment of nuclear SFs in the single-gluon-exchange PWIA approximation. That approach leads to a generalized convolution of distribution functions much like Eq. (1.3), with a simple correspondence between the featured quantities in the two representations [46,47].

This approach can actually be extended beyond single gluon exchange, and one shows that at least some higher-order QCD corrections can still be accommodated in a convolution [48]. In fact, formally the same expression (1.3) holds in both a hadronic and a QCD representation for F^A, provided one reinterprets $f^{A,\mathrm{PN}}$ in the latter as the distribution function of (centers of) nucleons in the target. It is not likely that there are significant QCD contributions that cannot be accommodated in a convolution. At the end of Sec. II we recalled and actually compared EMC ratios calculated in the hadron and in a parton representation.

The availability of planned Rosenbluth-separated data naturally simplifies the analysis, but will probably not resolve the exposed problems, as long as the scatter of neighboring points is much larger than the accuracy of each point. For instance, α_n extracted from Eq. (3.1) will remain sensitive to the input.

Use of the the same analyzing tools as before indicates that the new JLab data do not confirm previous conclusions, and, related to this, one cannot extract statistically significant information on the neutron, in contrast to the apparent success previously obtained from the OD. A resolution of this difficulty is clearly highly desirable.

ACKNOWLEDGMENTS

The authors are grateful to John Arrington, who provided us with all measured total inclusive cross sections, whether final or not, and made useful remarks. Thanks are equally due to Gianni Salme, who provided the three sets of $A = 3$ spectral functions, which enabled a realistic calculation of SFs for the $A = 3$ system.

APPENDIX

We start with a QCD prediction for the lowest moment $M_0(Q^2) = \int_0^1 dx\, F_2^p(x, Q^2) = 0.1471$ of a nuclear SF in the Bjorken limit with $N_f = 6$ contributing flavors. For any nuclear target a similar moment can be computed, given a parton representation of F_2^A. For several A and finite $Q^2 = (2.5\text{–}10.0)\ \mathrm{GeV}^2$, we found values up to 5%–6% lower than for a p [49].

We now add the moments of the computed $F_2^{^3\mathrm{He}}$ to previously reported results for $\langle N\rangle$, ^{2}H, ^{4}He, C, and Fe in Table I, Ref. [49]. For low $Q^2 \approx 2.5\ \mathrm{GeV}^2$ the moment of ^{3}He is 16% higher than for a p. That moment rapidly decreases with increasing Q^2 and becomes 0.1476 for $Q^2 = 10\ \mathrm{GeV}^2$, close to the Bjorken limit. That for ^{3}H is substantially closer to the previously computed moments of other light and medium-weight targets. As Fig. 5 illustrates, this is because of the differences of $f_{p,n}$ and of each distribution function for ^{3}He and ^{3}H. This also causes the differences in the predicted EMC ratios $\mu^{A=3}$.

We return to f^A in Eqs. (2.2) and (2.3), which we termed the SF of a fictitious nucleus composed of a point nucleus or, alternatively, a distribution function for the centers of nucleons in a nucleus. QCD is clearly not applicable to these artifacts, no matter how high Q^2 is. Their norm $\mathcal{N}$, very close to 1, differs from M_0^A of physical nuclei.

In Sec. II B we mentioned that, for either choice of NN interaction B2 or B2 + B3, the norm of the lowest-order part $\mathcal{N}_x(Q^2) = \int_0^3 dx f_{p,n}^{(0);A=3}(x, Q^2)$ equals 1 within a few parts per mille: More precisely, for $Q^2 = (2.5\text{–}10.0)\ \mathrm{GeV}^2$, $\mathcal{N}_x$ has a minute slope $\approx 0.0024/\mathrm{GeV}^2$. The same holds for $\mathcal{N}_y(q) = \int_{-q/2}^{q_{\max}} dy\, \phi^{(0)}(q, y)$.

For finite Q^2 the deviations of the norm from 1 and the minute slope of those deviations as a function of Q^2 are not due to numerical inaccuracies. We note that a total disregard of the missing energy and momentum yields $f(x, Q^2) = \delta(x - 1)$.

It is interesting to observe that the relevant missing energies appear restricted to $-|B_{^2\mathrm{H}}| \lesssim E/M \lesssim 0.012$, a range that dominates the underlying SPFT $S_{p,n}^{A=3}(k, E)$ (negative values occur only for a ^{2}H spectator). To a less extreme extent the same holds for the missing momentum: $k/M \lesssim 0.2$. Reinstatement of finite small missing energies and momenta produces distribution functions with finite Q^2-dependent widths.

This paper emphasizes $A = 3$ nuclei, but several points hold for general A. For ^{2}H a norm of 1 is trivial, but a similar observation can and has been made for ^{4}He, for which the underlying SPFT is fairly accurately known [22]. For heavier nuclei with models for ρ_2^A [see Ref. [22], Eqs. (9) and (10)], the norm $\mathcal{N}(f)$, when necessary, has been adjusted to 1.

Finally, the discussion holds for the lowest-order part $f^{(0)}$. For the reasons mentioned, it is not evident that, when FSI contributions are included, one should apply a small renormalization correction, owing to the relatively small $f^{A=3;(1)} \ll f^{A=3;(0)}$. We have not done so in our calculations.

[1] I. Niculescu *et al.*, Phys. Rev. Lett. **85**, 1182 (2000).
[2] J. Arrington *et al.*, Phys. Rev. C **64**, 014602 (2001).
[3] S. Rock *et al.*, Phys. Rev. Lett. **49**, 1139 (1982); Phys. Rev. D **46**, 24 (1992).
[4] D. B. Day *et al.*, Phys. Rev. C **48**, 1849 (1993).
[5] J. Arrington *et al.*, Phys. Rev. Lett. **82**, 2056 (1999); Phys. Rev. C **53**, 2248 (1996).
[6] J. Seely *et al.*, Phys. Rev. Lett., **103**, 202301 (2010).
[7] J. Arrington and D. Gaskell (private communication); [www.jlab.org/∼gaskelld/XEMPT/lightnuclei_paper/cross_sections].
[8] P. Solvignon, presented at ETC* Workshop, June 4–9 2008, Trento, Italy (unpublished).
[9] O. Benhar, A. Fabrocini, S. Fantoni, G. A. Miller, V. R. Pandharipande, and I. Sick, Phys. Rev. C **44**, 2328 (1991); O. Benhar *et al.*, Phys. Lett. B **489**, 131 (2000); M. Petraki, E. Mavrommatis, O. Benhar, J. W. Clark, A. Fabrocini, and S. Fantoni, Phys. Rev. C **67**, 014605 (2003).
[10] P. Fernandez de Cordoba *et al.*, Nucl. Phys. A **611**, 514 (1996).
[11] A. S. Rinat and M. F. Taragin, Nucl. Phys. A **571**, 733 (1994); **598**, 349 (1996); **620**, 417 (1997); **624**, 773(E) (1997); Phys. Rev. C **60**, 044601 (1999).
[12] S. A. Gurvitz and A. S. Rinat, Phys. Rev. C **65**, 024310 (2002).
[13] M. Osipenko *et al.*, Report No. CLAS-NOTE-2005-013, arXiv:hep-ph/0506004; Phys. Rev. C **73**, 045205 (2006); M. Kirch, P. V. Pobylitsa, and K. Goeke, Phys. Rev. D **72**, 054019 (2005).
[14] S. V. Akulinichev, S. A. Kulagin, and G. M. Vagradov, Phys. Lett. B **158**, 485 (1985).
[15] G. B. West, Ann. Phys. (NY) **74**, 464 (1972); W. B. Atwood and G. B. West, Phys. Rev. D **7**, 773 (1973).
[16] M. M. Sargsian, S. Simula, and M. I. Strikman, Phys. Rev. C **66**, 024001 (2002).
[17] S. A. Kulagin, G. Piller, and W. Weise, Phys. Rev. C **50**, 1154 (1994); S. A. Kulagin, *ibid.* **59**, 1722 (1999); G. Piller and W. Weise, Phys. Rep. **330**, 1 (2000).
[18] Y. Liang *et al.*, arXiv:nucl-ex/0410027; M. E. Christy (private communication). See also [hallcweb.jlab.org/res].
[19] M. Arneodo *et al.*, Phys. Lett. B **364**, 107 (1995).
[20] A. S. Rinat and M. F. Taragin, Phys. Lett. B **551**, 284 (2003).
[21] A. S. Rinat and B. K. Jennings, Phys. Rev. C **59**, 3371 (1999).
[22] M. Viviani, A. Kievsky, and A. S. Rinat, Phys. Rev. C **67**, 034003 (2003).
[23] S. A. Gurvitz, Phys. Rev. C **42**, 2653 (1990).
[24] J. Negele and D. Vautherin, Phys. Rev. C **5**, 1472 (1972); Nucl. Phys. A **549**, 498 (1992).
[25] A. S. Rinat, M. F. Taragin, and M. Viviani, Phys. Rev. C **70**, 014003 (2004); Nucl. Phys. A **784**, 25 (2007).
[26] M. Jones *et al.*, Phys. Rev. Lett. **84**, 1398 (2000); in *Proceedings of the Third Workshop on Perspective in Hadronic Physics, Trieste*, 2001; Nucl. Phys. A **699**, 124c (2002); Phys. Rev. Lett. **88**, 092301 (2002).
[27] P. A. M. Guichon and M. Vanderhaeghen, Phys. Rev. Lett. **91**, 142303 (2003); Y. C. Chen, A. Afanasev, S. J. Brodsky, C. E. Carlson, and M. Vanderhaeghen, *ibid.* **93**, 122301 (2004); P. G. Blunden, W. Melnitchouk, and J. A. Tjon, Phys. Rev. C **72**, 034612 (2005).
[28] J. Arrington, W. Melnitchouk, and J. A. Tjon, Phys. Rev. C **76**, 035205 (2007).
[29] H. de Vries *et al.*, At. Nucl. Tables **36**, 496 (1987), Tables IV and V.
[30] A. Kievsky, E. Pace, G. Salme, and M. Viviani, Phys. Rev. C **56**, 64 (1997).
[31] R. B. Wiringa, V. G. J. Stoks, and R. Schiavilla, Phys. Rev. C **51**, 38 (1995).
[32] B. S. Pudliner *et al.*, Phys. Rev. C **56**, 1720 (1997).
[33] A. S. Rinat, M. F. Taragin, and M. Viviani, Phys. Rev. C **72**, 015211 (2005).
[34] S. A. Kulagin and R. Petti, Nucl. Phys. A **765**, 126 (2006).
[35] G. G. Petratos *et al.*, in *Proceedings of the Workshop on Experiments with Tritium at JLab, 1999* (Jefferson Lab, Newport News, 1999).
[36] E. Pace, G. Salme, S. Scopetta, and A. Kievsky, Phys. Rev. C **64**, 055203 (2001); Nucl. Phys. A **689**, 453 (2001).
[37] I. R. Afnan *et al.*, Phys. Rev. C **68**, 035201 (2003).
[38] W. Brooks, Nucl. Phys. A **755**, 261 (2005); J. Lachniet *et al.*, Phys. Rev. Lett. **102**, 192001 (2009).
[39] A. Lung *et al.*, Phys. Rev. Lett. **70**, 718 (1993).
[40] J. P. B. C. Melo *et al.*, Phys. Lett. B **671**, 153 (2009).
[41] W. Melnitchouk and A. W. Thomas, Phys. Lett. B **377**, 11 (1996).
[42] Y. Kahn, W. Melnitchuk, and S. A. Kulagin, Phys. Rev. C **79**, 035205 (2009).
[43] J. Arrington, F. Coester, R. J. Holt, and T.-S. Lee, J. Phys. G **36**, 025005 (2009).
[44] M. Osipenko *et al.*, Nucl. Phys. A **766**, 142 (2006).
[45] J. Arrington (private communication).
[46] R. L. Jaffe, in *Proceedings of the Los Alamos Summer School, 1985*, edited by M. Johnson and A. Picklesimer (Wiley, New York, 1986).
[47] G. B. West, in *Interactions between Particles and Nuclear Physics*, edited by R. E. Mischke (AIP, New York, 1984), p. 360.
[48] A. S. Rinat and M. F. Taragin, Phys. Rev. C **73**, 045201 (2006).
[49] A. S. Rinat and M. F. Taragin, Phys. Rev. C **72**, 065209 (2005).